



Walter Schottky Institut
Center for Nanotechnology and Nanomaterials
Fakultät für Physik der Technischen Universität München

Electrical Readout of NV⁻ Centers in Diamond

Felix Nikolaus Hartz

Master Thesis

September 2017

Zusammenfassung

Das einfach negativ geladene NV⁻-Zentrum in Diamant besteht aus einem Stickstoffatom an einem Kohlenstoff-Gitterplatz und einer benachbarten Leerstelle und wird sowohl im Bereich der Quantensensorik als auch zur Speicherung und Verarbeitung von Quanteninformation verwendet. Das Spin-1-System dieses Defekts weist hohe Elektronenspindichten auf. In dieser Arbeit wird ein elektrisches Ausleseverfahren als Alternative zu den bisher verwendeten optischen Verfahren diskutiert. Dieses Verfahren basiert auf einer photoinduzierten Ionisation des NV⁻-Zentrums, deren Effizienz abhängt vom Spinzustand des Zentrums. Die Spindynamik ist dabei ein Ergebnis der komplexen Dynamik der angeregten Zustände des NV⁻-Zentrums. Eine Apparatur zur experimentellen Untersuchung der Photoleitfähigkeit von Diamant wurde im Rahmen dieser Arbeit aufgebaut. Mittels resonanter Mikrowelleneinstrahlung konnte der Spinzustand der NV⁻-Zentren eingestellt werden und die daraus resultierende Reduktion des Photostroms beobachtet werden. Die Optimierung der dazu verwendeten optischen und Mikrowellen-Pulse konnte institutsinterne Vorarbeiten reproduzieren. Erste Studien zu Pulsprotokollen, in denen die optische Anregung mit Photonen unterschiedlicher Wellenlänge durchgeführt wird, werden vorgestellt.

Contents

1 NV⁻ Center in Diamond as a Future Quantum Memory Candidate	1
2 Theory	3
2.1 High Purity Single Crystal Diamond	3
2.1.1 NV ⁻ Centers in Diamond	3
2.1.2 NV ⁻ Center Level Diagram and Photoluminescence Spectrum . . .	4
2.1.3 Generation of Photocurrent in Diamond	5
2.2 Electron Spin Resonance	6
2.2.1 Rotating Frame System	7
2.3 Metal-Semiconductor-Metal Photodetector Operation Principle	9
3 Diamond Samples	13
3.1 Single Crystal Diamond Substrates	13
3.2 Sample Processing	13
3.3 Current-Voltage Characteristics	16
4 Experimental Setup for pEDMR and ODMR Detection of NV⁻ Centers in Diamond	19
4.1 Optics	20
4.1.1 Laser Sources	20
4.1.2 Confocal Microscopy	21
4.1.3 Single Photon Avalanche Detector for NV ⁻ Fluorescence Detection	24
4.2 Electronics	25
4.2.1 Low Noise Transimpedance Amplifier for Photocurrent Detection	25
4.2.2 Microwave Circuit	26
4.3 Timing Control	27
5 Basic Experiments	31
5.1 Photoluminescence Detection and ODMR of NV ⁻ Centers	31
5.1.1 Spatial Resolution of the Photoluminescence Detection	32
5.1.2 ODMR on NV ⁻ Centers	33

5.2	Photocurrent Detection	36
5.2.1	Two Photon Ionization of the NV ⁻ Center	36
5.2.2	Characteristics of the MSM Photodetector	38
5.2.3	Mapping the Photocurrent	40
5.3	Pulsed Electrical Detected Magnetic Resonance on NV ⁻ Centers	42
5.3.1	Electron Spin Resonance	42
5.3.2	Optimization of pEDMR Dynamics	45
6	Dual Laser Excitation of the NV⁻ Center	49
6.1	520 nm and 450 nm Dual Laser NV ⁻ Ionization	49
6.1.1	Alignment of Laser Spots	49
6.1.2	450 nm Laser Photoionization of the NV ⁻ Center	51
6.1.3	Pulse Sequence for Green and Blue Laser Assisted pEDMR on NV ⁻ Centers	53
6.2	Discussion of a Dual Laser Photoionization Protocol prohibiting N _s ⁰ Ionization	58
6.2.1	Laser Alignment	58
6.2.2	Green Near-Infrared Pulse Sequence	60
7	Conclusions and Outlook	63
A	Laser Characteristics	67
A.1	Mathematical Discussion on Laser Calibration	67
A.2	Laser Power Calibration	69
A.3	Laser Suppression in the Photon Detection System	69

Chapter 1

NV⁻ Center in Diamond as a Future Quantum Memory Candidate

With increasing interest research on the diamond nitrogen vacancy (NV⁻) center has been conducted for more than a decade. Alternatives for the well understood and utilized silicon-based transistor technology are searched for by scientists also with rising financial support from computer industry. As one of the more abundant defects in natural diamond the NV⁻ center forms a paramagnetic spin triplet with excellent spin coherence times providing quantum information storage at room temperature [1]. The spin of NV⁻ centers can be manipulated thousands of times before decoherence sets a limit to further operation. Without nuclear spins disturbing electron spin coherence silicon and diamond are candidates for implementing single qubits into semiconductor environment [2]. Isotope enrichment of ²⁸Si or ¹²C can provide these nuclear spin free environments. Ultimately, electronic fluctuations at surfaces limit the coherence [3]. The NV⁻ center can be utilized as a quantum sensor demonstrating good performance and sensitivity when detecting temperature, electric or magnetic fields [4], [5], [6]. The level splitting of the NV⁻ center spin in its ground state is sensitive to all three mentioned quantities and even allows to identify the field orientation with respect to the orientation of the NV⁻ center in the diamond lattice. Recent studies demonstrated the experimental reconstruction of magnetic fields generated by small magnetic samples attached to a diamond surface [7].

The spin of NV⁻ centers can be read out optically with well established photoluminescence detection techniques, typically using the same objective for detection as for excitation. Outcoupling of photons from highly refractive diamond into air is small and a variety of concepts for the optimization of photon outcoupling is discussed. While Purcell effect increases the photon count rate at the cost of spin contrast, additional optics such as mirrors, micro-antennas, oil and solid immersion lenses and dielectric or plasmonic grating enhance photon collection efficiency [8], [9]. A very different approach

to study NV⁻ center spin and charge is electrical detecton with picosecond resolution, when the NV⁻ center is coupled to graphene [10]. Spin selectivity is here provided by graphene. The spin state of a NV⁻ center may be read out as well by fabricating metallic contacts, effectively creating a metal-semiconductor-metal photo-detector. This ansatz allows for downscaling and has been demonstrated to provide results that compare with photoluminescence detection [11], [12]. The physics of electrical readout is more complex and understood as an effective four photon absorption process that can be driven at least at wavelengths in the green part of the electromagnetic spectrum. In this work we will discuss this process and possibilities for optimization. All experimental findings can be explained by a model of the NV⁻ center that is in agreement with other reports on theoretical and experimental studies.

Chapter 2

Theory

2.1 High Purity Single Crystal Diamond

Diamonds can exhibit notable differences in their physical properties. In particular, the conduction may vary from insulating over n- or p-type bulk semiconductivity, surface-type conductivity to superconductivity [13], [14]. Since impurities and defects define the electrical properties as well as, in the case of photoconductivity, optical absorption, the entire field of research benefits from advanced materials engineering e.g. in the chemical vapour deposition (CVD) diamond growth process [15]. Further tuning the electronic structure through surface states beyond introducing impurities in the bulk enables construction of a new generation of devices based on diamond such as field effect transistors (FETs) [13].

2.1.1 NV⁻ Centers in Diamond

The four carbon valence electrons form covalent sp³ bonds [16]. The resulting crystal structure is a face centered cubic with a base formed by two atoms, known as the diamond structure. All bonds have the same length and occur under the tetrahedral angle of 109.5°. Diamond exhibits an indirect bandgap of 5.45 eV [16]. Due to the high binding energy of the bonds diamond holds the record in mechanical stability, heat conductivity and predicted breakdown voltages of ~ 10 MV/cm [15], [5].

In combination with an acceptably electron mobility of up to 4500 cm²/Vs in single crystal diamonds (SCD) even at room temperature and above scientific research interest in diamond-based devices rises [15]. Motivated by the discovery along spin coherence time also at room temperature diamond is a possible candidate for future quantum information processing [1]. Naturally abundant diamonds have a varying density and distribution of impurities. This led to a classification system used today, albeit the criteria changed over time with increasing knowledge and technology progress [17]. Table 2.1

type	characteristic feature	[N] (cm ⁻³)
Ia	N clusters	$\approx 2 \cdot 10^{18} - 5 \cdot 10^{20}$
Ib	low N	$\approx 4 - 9 \cdot 10^{19}$
IIa	N	$< 2 \cdot 10^{18}$
IIb	hardly detectable N	$< 2 \cdot 10^{16}$

Table 2.1: Classification of diamond types [17].

gives an overview of the different diamond types.

The samples used in this work were type IIa SCDs with nitrogen concentrations ([N]) in bulk material of $[N] \leq 2 \cdot 10^{19}$ cm⁻³. At room temperature and elevated temperatures the carrier mobility for type IIa diamonds is limited by acoustic phonon scattering, as has been concluded from time of flight measurements where the current transient of a pulsed, optically induced photocurrent has been analysed [15]. Different electron mobilities between 2000-2800 cm²/Vs for type IIa diamonds and 4100 cm²/Vs in SCDs are attributed to a different extent of defect-scattering, still being minimized with crystal quality [15]. Due to the higher effective mass hole mobility is lower, typically by 20%. NV⁻ center defects are randomly distributed in the sample and occur wherever one nitrogen donor is next neighbour to one carbon vacancy. In the following section the physical properties of the NV⁻ center will be described.

2.1.2 NV⁻ Center Level Diagram and Photoluminescence Spectrum

The level diagram of the NV⁻ center is shown in Fig. 2.1 b) and the spin density corresponding to the ground state in Fig. 2.1 a). We define states $|1\rangle$, $|2\rangle$ as the optical ground state and $|3\rangle$, $|4\rangle$ as optical excited state of the NV⁻ center and name $|5\rangle$ its dark state. We call the lifetime corresponding to state $|i\rangle$ τ_i and will also consider partial lifetimes τ_{ij} as the inverse of the transition rate from state $|i\rangle$ into $|j\rangle$ [16]. The overall lifetimes is related to radiative and nonradiative lifetimes, in the case of state $|3\rangle$ by [16]

$$\frac{1}{\tau_3} = \frac{1}{\tau_{31}} + \frac{1}{\tau_{35}}. \quad (2.1)$$

Partial lifetimes obtained from fits to experimental data and are provided in Tab. 2.2 [18].

The optical ground state exhibits a zero-field splitting D between states $|1\rangle$ and $|2\rangle$. Excitation with green laser light promotes a valence electron into the phonon side band of one of the optically excited states. For this electrical transition (E1) spin is conserved. Radiative relaxation to the initial states occurs with a transition rate of 15.8 ns or 15.9

state	radiative lifetime (ns)	nonradiative lifetime (ns)
$ 3\rangle$	$\tau_{31} = 15.8$ ns	$\tau_{35} = 77.1$ ns
$ 4\rangle$	$\tau_{42} = 15.9$ ns	$\tau_{45} = 12.9$ ns
$ 5\rangle$	-	$\tau_{51} = 289$ ns, $\tau_{52} = 463$ ns

Table 2.2: Partial lifetimes of the excited NV⁻ center. Data is taken from Robledo [18].

ns, slightly depending on the spin [12]. The photoluminescence spectrum arising from this NV⁻ center transition as depicted in green in Fig. 2.1 c) is known for more than two decades [19], [20]. There is another decay channel into a non-photoluminescent state $|5\rangle$, also referred to as dark state. Nonradiative transition rates into the dark state strongly depend on the spin, with $\tau_{35} = 77.1$ ns being slower or with $\tau_{45} = 12.9$ ns being faster than the radiative decay with $\tau \approx 16$ ns. However, the NV⁻ center spin is not conserved in this nonradiative transition. Relaxation from $|5\rangle$ back to the optical ground state takes significantly longer than the prior transitions.

The photoluminescence spectra of both NV center charge states are depicted in Fig. 2.1 c), adapted from [19]. Dependent on the wavelength of the laser used for excitation the NV⁻ center is preferably in its neutral or singly negatively charged state. Under 440 nm laser excitation the neutral charge state gets excited and relaxes by photoluminescence. The zero photon line (ZPL) for NV⁰ can be observed as a sharp maximum at the high energy side of the spectrum, the value is reported to be 575 nm. NV⁻ center photoluminescence cannot be detected, when the laser photon energy is lower than the NV⁰ ZPL and thus cannot excite NV⁰. The photoluminescence spectrum of NV⁻, here recorded under 514 nm laser excitation into the phonon side band, reveals the weak ZPL at 637 nm. Emission into the phonon side band is much more probable. The spectrum is centered at about 700 nm and has a width at half maximum of about 80 μ m.

2.1.3 Generation of Photocurrent in Diamond

Ionization of the NV⁻ center occurs when the energy of the exciting photons exceeds the ZPL transition energy. A process including three photons is considered to drive the ionization as has been proposed by [22].

In Fig. 2.2 a) the NV⁻ center level structure and the individual excitation steps are depicted. Four of the six valence electrons of the NV⁻ center populate two highly symmetric orbitals (a_1), where one of these lies in the valence band [22]. The remaining two electrons occupy different orbitals, that exhibit lower symmetry (e) and are energetically

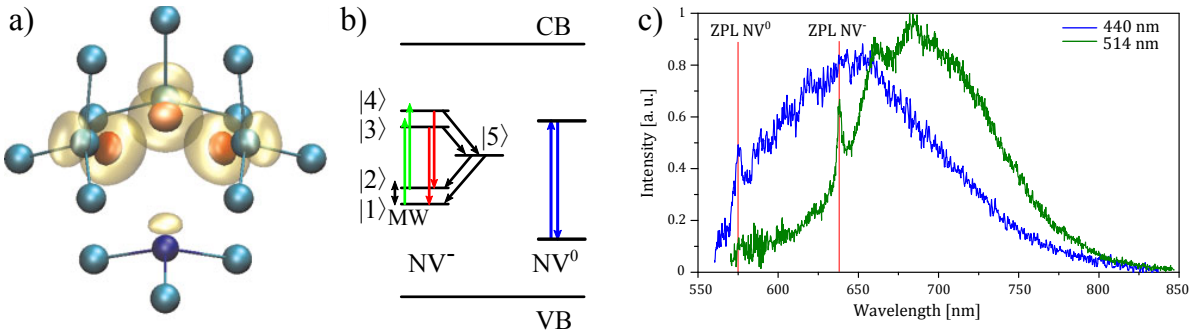


Figure 2.1: (a) Structure of the NV^- center in diamond and the simulated spin density contour [21]. b) Level scheme with indicated microwave and optical photon transitions. c) Photoluminescence spectra for both NV^0 and NV^- centers recorded with different excitation energies [19]

higher than the a_1 energy levels. The initial spin configuration of spin one results from two up spins in the e orbitals, corresponding to state $|2\rangle$ in our nomenclature. From the a_1 orbital in the band gap a first photon promotes one electron into the first optically excited state, $|4\rangle$. A second photon lifts this electron into the conduction band before relaxation into the ground or dark state. From density functional theory simulations it is conducted, that an Auger process takes place on a faster timescale than relaxation [22]. The result is a high energy electron in the conduction band that has sufficient energy to leave the defect. When the conduction band electron has escaped, the defect is in its neutral state NV^0 . Under illumination the initial negative charge state is restored, as shown in Fig. 2.2 b). An electron of the a_1 orbital in the band gap is excited and a_1 is subsequently refilled by a valence band electron. This leaves a hole state in the valence band which can propagate to a contact. We end up after one cycle with the initial NV^- state having created a free electron and a free hole.

2.2 Electron Spin Resonance

Six electrons build up the NV^- center in diamond exhibiting a spin of one. For the magnetic interaction of the spin with its environment one considers the spin Hamiltonian in the optical ground state. It is the sum of the Zeeman term and a finestructure contribution [23]

$$H = \mu_b g \mathbf{S} \mathbf{B}_0 + \mathbf{S} \hat{\mathbf{D}} \mathbf{S}. \quad (2.2)$$

Here g denotes the g factor of the electron, μ_b the Bohr magneton, \mathbf{S} the total electron spin, \mathbf{B}_0 the static external magnetic field and $\hat{\mathbf{D}}$ the zero-field splitting tensor.

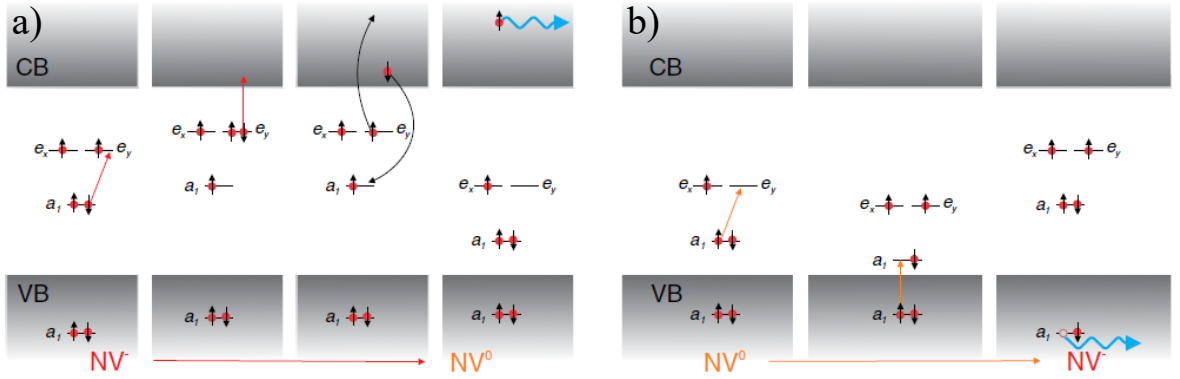


Figure 2.2: a) Ionization of the NV^- center by two photon excitation. b) The initial negative charge state is restored by two photon excitation of a valence band electron [22]. Energy level differences for varying orbital occupation or charge-state are illustrated schematically only.

In absence of any magnetic field the Zeeman term vanishes and one obtains

$$H = D \left(S_z^2 - \frac{1}{3}S(S+1) \right) + E(S_x^2 + S_y^2) \quad (2.3)$$

with the zero-field splitting parameter $D = 3/2 D_{zz}$ [23]. For crystals like diamond with C_{3v} symmetry there is no anisotropy field and thus $E = 0$, simplifying (2.3) to

$$H = D \left(S_z^2 - \frac{1}{3}S(S+1) \right). \quad (2.4)$$

Therefore, we expect for the different spin states with the projections $S_z = 0$ and $S_z = \pm 1$ an energy difference of D .

2.2.1 Rotating Frame System

So far we have discussed spin precession in a constant magnetic field. Transitions between spin states can be induced by microwave photons of the right frequency and polarization. In this section the mathematical representation of the spin state will be discussed under the influence of an additional magnetic microwave field. The Schrödinger equation of a spin system being driven by a time-dependent magnetic field B_{MW} shows a time dependence as well [24]. By appropriate choice of coordinate system this time dependence disappears. This is the case for coordinate axes rotating along the quantization axis z with Larmor frequency ω_0 , as illustrated in Fig. 2.3 a) and b).

In the rotating frame system the hamiltonian includes an operator rotating the spin state along the x -axis (\hat{I}_x), as depicted schematically in Fig. 2.3 c) [24]. The frequency of rotation is called nutation frequency which is direct proportional to B_{MW}

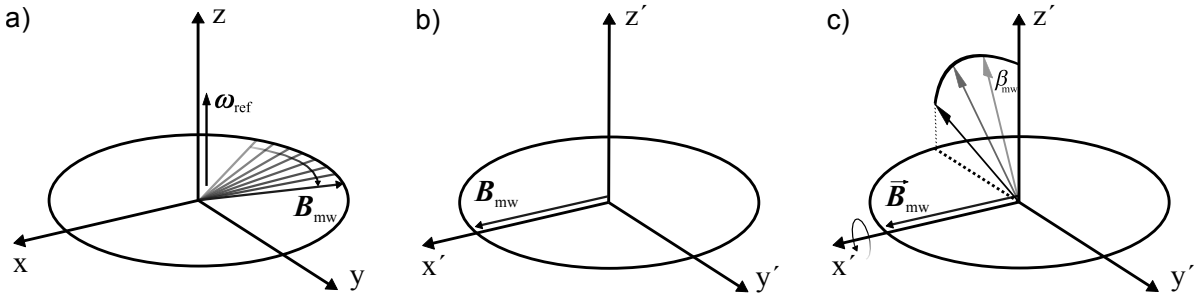


Figure 2.3: a) In the laboratory frame system \mathbf{B}_{MW} precesses, whereas b) \mathbf{B}_{MW} has a time independent representation in a rotating frame system where ω_{ref} is set to ω_0 . c) A microwave pulse rotates the spin state along the x axis into another z projection state.

with [24]

$$\hbar\omega_{\text{nut}} = g\mu_{\text{b}}B_{\text{MW}}. \quad (2.5)$$

The operator \hat{I}_x rotates the spin state around the x -axis by a rotation angle β_{MW} for a constant magnetic field actioning over the time of the microwave pulse (t_{MW}) [24]

$$\beta_{\text{MW}} = \omega_{\text{nut}}t_{\text{MW}}. \quad (2.6)$$

Experimentally spin transitions are of interest in this work, in particular the rotation by $\beta_{\text{MW}} = \pi$. The corresponding interaction time can be estimated from the experimentally available magnetic field that is provided by a gold wire. It has a diameter of $70 \mu\text{m}$ and is placed close to the interdigital contact structure. In reality the skin effect defines the penetration depth in metals, described by the skin depth as characteristic parameter. The choice of the wire radius is a trade-off between high radiation efficiency, a large cross section for current transport at microwave frequencies and small wire to probe volume distance to maximize the magnetic field. From the Biot-Savart law one can derive easily the magnetic field B_{MW} for the two-dimensional and radial-symmetric case

$$B_{\text{MW}}(R) = \frac{\mu_0 I}{2\pi R}. \quad (2.7)$$

Here, R denotes the distance to the wire center and I the total current through the wire. We neglect the direct current (DC) resistance and use the impedance $R_z = 50 \Omega$ for an estimation of B_{MW} . Under laboratory conditions we typically operate with a microwave power of 10 W at a distance of $70 \mu\text{m}$ to the wire center. From these experimental parameters we obtain with (2.7) an estimate for B_{MW} considerably close to the wire

$$B_{\text{MW}} = \frac{\mu_0 \sqrt{P/R_z}}{2\pi R} = \frac{\mu_0 \sqrt{10 \text{ W}/50 \Omega}}{2\pi \cdot 70 \mu\text{m}} = 1.3 \text{ mT}. \quad (2.8)$$

Using (2.5) and (2.6) we can convert B_{MW} into $\omega_{\text{nut}} = 2.9 \text{ MHz}$ and finally obtain for the spin flip time $t_{\text{MW}} = 170 \text{ ns}$.

2.3 Metal-Semiconductor-Metal Photodetector Operation Principle

Experimentally the task is to detect a photocurrent generated in bulk diamond. Evaporated metallic contacts on the diamond surface allow detection of a photocurrent when a bias voltage is applied to the device. The device concept used is that of a metal-semiconductor-metal (MSM) photodetector. In this section we will discuss the relevant physical properties and limits of the in house-built MSM detectors.

The general device structure consists of interdigital contacts directly on the sample surface, possibly with a barrier enhancing layer in between [16]. In the region between the contacts a volume of detector material is illuminated and charge carriers are excited. In biased operation mode a depletion region is build at the anode effectively separating the generated charge carriers. Under the influence of the electrical field they drift to the contacts. This process is illustrated schematically in Fig. 2.4 for a structure with contact width w and contact spacing s .

With increasing bias voltage the depletion region expands. In one dimensional approximation the depletion region (w_{dep}) can be calculated following [16]

$$w_{\text{dep}} = \sqrt{\frac{2\epsilon_s U_b}{qN}}. \quad (2.9)$$

Here ϵ_s and N denote the effective dielectric constant and the doping density, respectively. The depletion region increases with the square root of the bias voltage U_b . A saturation of photocurrent is expected when the entire region between contacts gets depleted by a voltage (U_{fb}) that can be expressed as

$$U_{\text{fb}} = \frac{qN}{2\epsilon_s} s^2. \quad (2.10)$$

In this case the band curvature at the anode is zero, referred to as flat-band mode. The MSM detector is read out by a low bandwidth transimpedance amplifier (TIA). When the TIA amplification is set to 10^{11} corresponding to an inner TIA resistance (R_i) of $100 \text{ G}\Omega$ a typically detected photocurrent in the order of 10 pA is amplified to a voltage signal of 1 V . Assuming a sample capacity (C_s) of 10 pA one obtains for the RC time constant (τ_{RC}) of the experiment [16]

$$\tau_{\text{RC}} = R_i C_s = 1 \text{ s}. \quad (2.11)$$

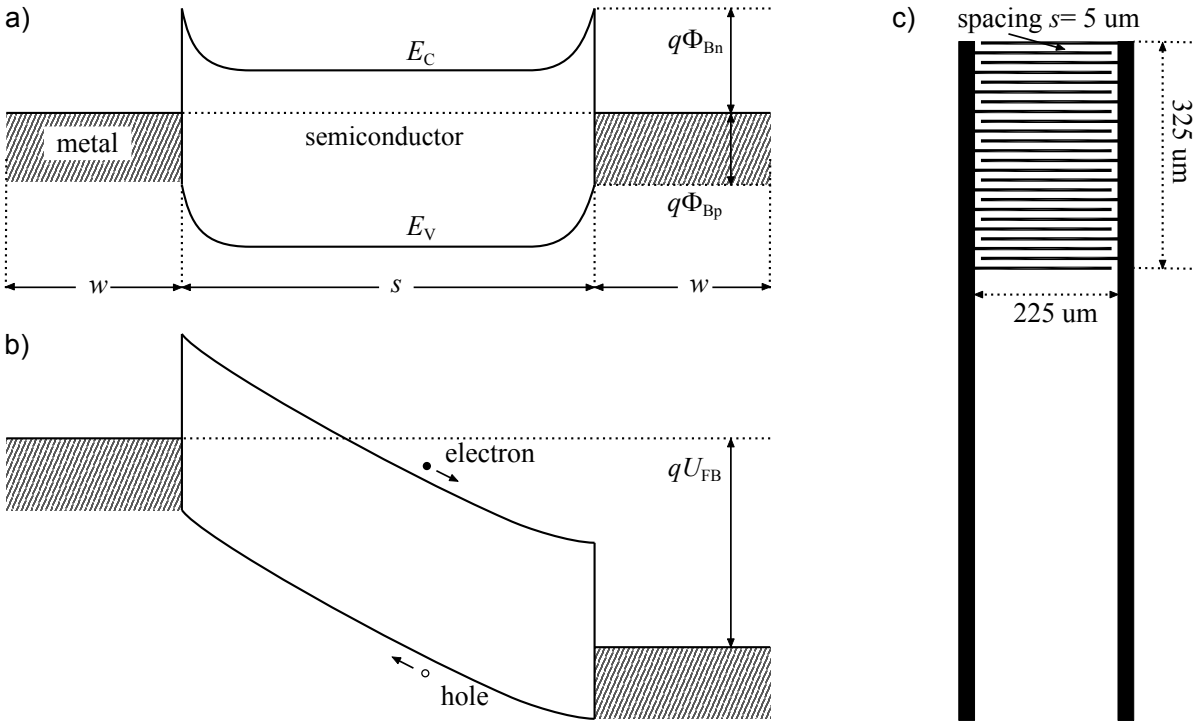


Figure 2.4: Band level scheme for a MSM photodetector in an a) unbiased configuration and for b) flat-band condition, where the electric field at the anode becomes zero. c) MSM detector layout with 24 interdigital contacts.

This τ_{RC} in the order of seconds effectively limits the readout speed, due to the high R_i of the TIA. For the experiments we use integration times between 0.05 s and up to 5 s for small photocurrent levels below 1 pA.

Ohmic Contacts on Diamond

Photoconductive Gain

Internal processes can lead to an observable current being higher than the current primarily generated by photoexcitation in the detector. This subsection refers to the discussion of Sze in [16]. The current enhancing effect is described by a photoconductive gain factor

$$G = \frac{I_p}{I_{ph}}. \quad (2.12)$$

Here the current generated by a photo excitation is denoted as I_{ph} and the detected current as I_p . Electrons and holes drift in an electric field to opposite contacts where they are collected. Characteristic are the carrier density n and the carrier lifetime τ , which depends on the position of the Fermi level and the relevant relaxation process

in the detector material of dimensions $A \cdot L = V$. Under constant carrier generation rate G_e for carriers with charge q the steady state condition for the carrier density is

$$n = G_e \tau \quad (2.13)$$

giving rise to a drift current in an electric field E of

$$I_p = (\mu_n + \mu_p) n q E A. \quad (2.14)$$

The primary photocurrent is just

$$I_{ph} = \frac{q G_e}{V}. \quad (2.15)$$

Inserting (2.14) and (2.15) in (2.12) yields

$$G = \frac{(\mu_n + \mu_p) \tau E}{L} = \tau \left(\frac{1}{\tau_n} + \frac{1}{\tau_p} \right). \quad (2.16)$$

Here the carrier transition times are defined as

$$\tau_{n,p} = \frac{L}{\mu_{n,p} E}, \quad (2.17)$$

scaling linearly with the distance of travel and inversely with the acceleration field below saturation.

Chapter 3

Diamond Samples

3.1 Single Crystal Diamond Substrates

As substrate we use chemical vapour-grown single crystal diamonds. They exhibit a homogeneously distributed nitrogen density of $[N] < 1$ ppm. Boron atoms with a concentration of $[B] < 5$ ppb are not the dominant defect. NV^- defects occur naturally at one percent of the nitrogen atoms in diamond. The ratio can be increased when defects in the diamond crystal are generated by irradiation with electrons or by nitrogen implantation [25], [26]. Without external magnetic field and thus without a well defined quantization axis it is not important how the crystal is aligned with respect to the setup geometry. We are free to choose any crystal orientation. However we choose the (100) surface orientation for all of our samples. The roughness of the polished diamond surface is specified to be less than 10 nm on average. These smooth surfaces provide a well defined starting point for further processing steps. A schematic overview of the fabrication processes is given in Fig. 3.1.

3.2 Sample Processing

Within the scope of this work four diamond samples varying in defect concentration and contact fabrication have been studied. By the choice of contact material the Schottky barrier height can be adjusted. Annealing of evaporated contacts reduces the barrier height again. Engineering of the required contacts is possible, however the goal was to realize samples with Schottky and others with ohmic contacts.

Sample Cleaning

The standard cleaning procedure is rinsing the sample with acetone, then with isopropanol and final drying with nitrogen gas. In case of metal contamination a hot bath

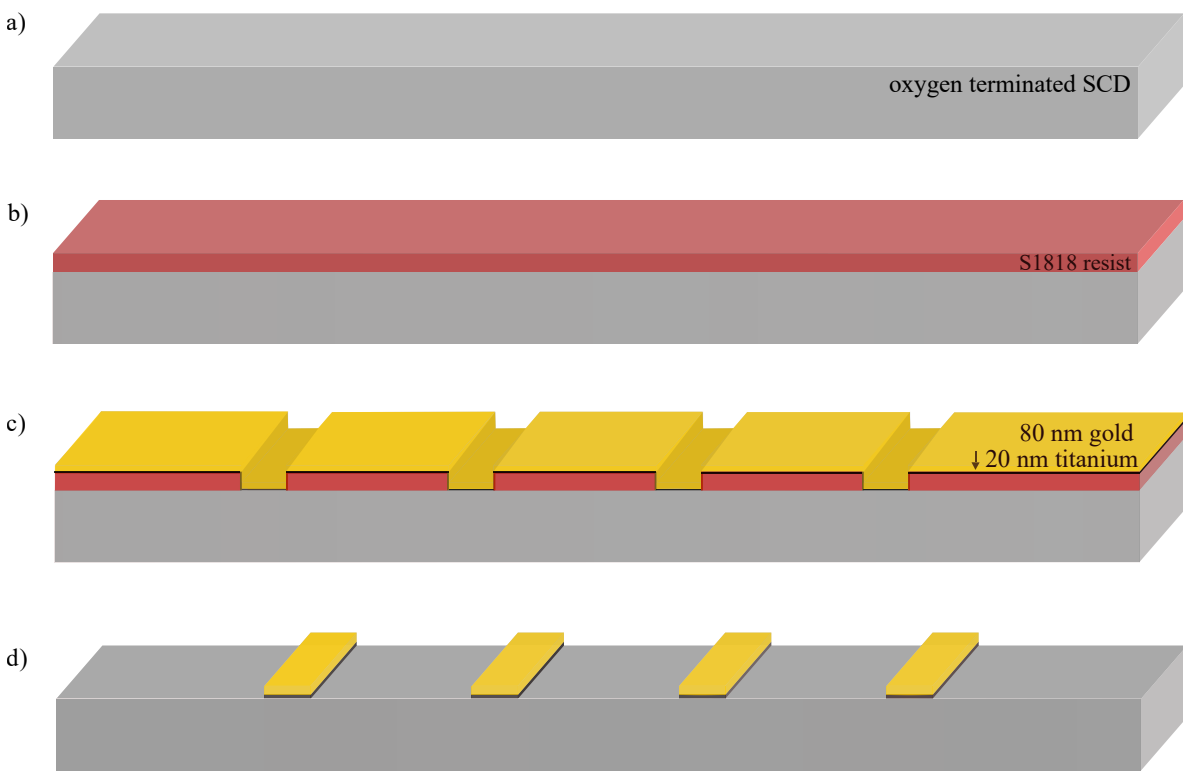


Figure 3.1: Contact fabrication. The diamond sample a) is covered by photoresist. b) After UV-lithography and metal evaporation c) the interdigitated structure d) is developed with a lift-off process.

of sulfuric acid and potassium nitrate is used to remove base metal traces and organic residues. Diamonds are boiled in etching bath consisting of 20 ml H₂SO₄ and two spatula tips of KNO₃ at 225 C for 60 min. Afterwards they are rinsed with deionised water.

Oxygen Termination of the Surface

The samples were oxygen plasma treated before and after the lithography step. This method provides a non-directional etching of surface contaminations on the diamond including hydrogen termination. Adhesion of metal contacts that are to be fabricated later on is improved as well. Dependent on power and duration of the microwave plasma the shape and etching depth can be tuned. The influence of these parameters on the resulting surface quality has been investigated and optimized by Hauf [13]. For the plasma microwave reactor used (*Technics Plasma GmbH 100-E Plasma System*) operation at 1.4 mbar and a power of 200 W for 300 s is the set of parameters promising good results [13].

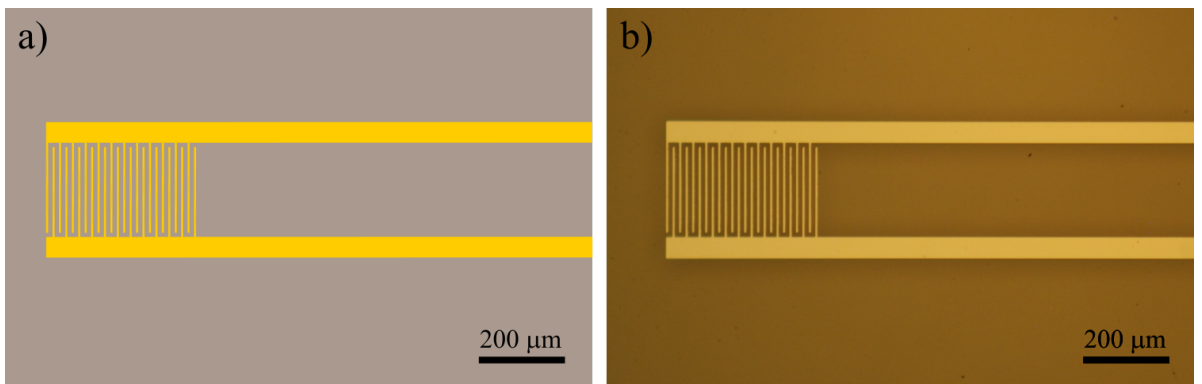


Figure 3.2: a) Schematic of the intended contact geometry and b) microscope image of sample O1 after the lift-off process.

UV-Photolithography

Metallic top contacts were fabricated using UV-photolithography. Two interdigital structures as introduced in section 2.3 with contact width of $5 \mu\text{m}$ and contact distance of $10 \mu\text{m}$ were used. Due to the limited charge carrier mobility in diamond we chose these small contact distances. Positive photoresist (*Schipley S1818*) is spun at 9000 rpm for 30 s. Before the pre-bake at 90°C for 10 min photoresist aggregated at the sample edges is removed with a razor blade. A mask aligner (*Karl Süss GmbH & Co. KG MJB3*) exposes the resist structure to a mercury lamp emission at wavelength $\lambda = 365 \text{ nm}$ for 6 s. Afterwards the development is performed in a 1:5 dilution of developer (*Rohm and Haas Company microposit Dev 351*) and water, usually for 15 s.

Metal Contact Fabrication

Electron beam evaporation was used for depositing 20 nm of titanium and 80 nm of gold on the oxygenated diamond surface for samples S1 and O2. Only for sample O1 contacts were evaporated thermally in a layer of 10 nm titanium and 80 nm aluminum, those parameters are adapted from a fabrication process resulting in ohmic contacts [11]. After evaporation of the metal contacts lift-off was performed in an ultrasonic acetone bath at room temperature. For treatment steps of two minutes the ultrasonic power was increased in small steps. All used parameters are summarized in Tab. 3.1. During metal evaporation an oxygen terminated surface allows formation of an oxide at the surface, resulting in an electrical contact and mechanical stability of the thin metal contact [13], [27].

sample	contact materials	thickness (nm)	annealing
S1, O2	Ti, Au	20, 80	no annealing
O1	Ti, Al	10, 80	3 h at 510 °C in vacuum

Table 3.1: *Contact materials of the diamond samples.*

Annealing of Contacts

Sample O2 was annealed after lift-off for three hours at 510 °C in vacuum. At this temperature aluminum diffuses into the gold and into the diamond surface decreasing the Schottky barrier height while mechanical stability is enhanced. Annealing was performed in a high vacuum oven providing a pressure below 3×10^{-6} mbar during the annealing process. Temperature was stabilized at a level of (510 ± 10) °C.

Processing Metal Contacts on Diamond

3.3 Current-Voltage Characteristics

Three different samples are presented within the scope of this work. The influence of the selected contact material on the Schottky barrier height of contacts on high purity diamonds has been investigated during the 1990s. Titanium gold contacts on diamond are reported to exhibit Schottky barrier heights of about 1 eV on oxygen terminated surfaces [27]. A small photocurrent, typically in the range of pA, is measured with a TIA as described in section 4.2. Samples are contacted with top contact electrodes processed as described in the previous section. Analysis of the current-voltage dependence allows for conclusions on conductivity and contact properties.

For the determination of the dark current in the samples room light was switched off. Remaining diffuse light sources like instrument's displays lead to a diffusive light intensity in the nW range, which was further reduced by additionally covering the sample. Without photoionization only the reverse bias current can contribute to the dark current in Schottky diodes. Basically, thermionic emission allows electrons with high kinetic energy to tunnel into the contacts. Results of the corresponding current voltage characteristic measurements, conducted at room temperature, are depicted in Fig. 3.3. Very long settling times for the current were observed, indicating that the experiment was not in a dark state equilibrium. The relaxation time of the charge carriers and thus Fermi level was reported to exceed hours for some diamond substrates with low carrier densities at room temperature, for varying illumination conditions [28]. The data recorded here serves just as an upper limit for the dark current U - I characteris-

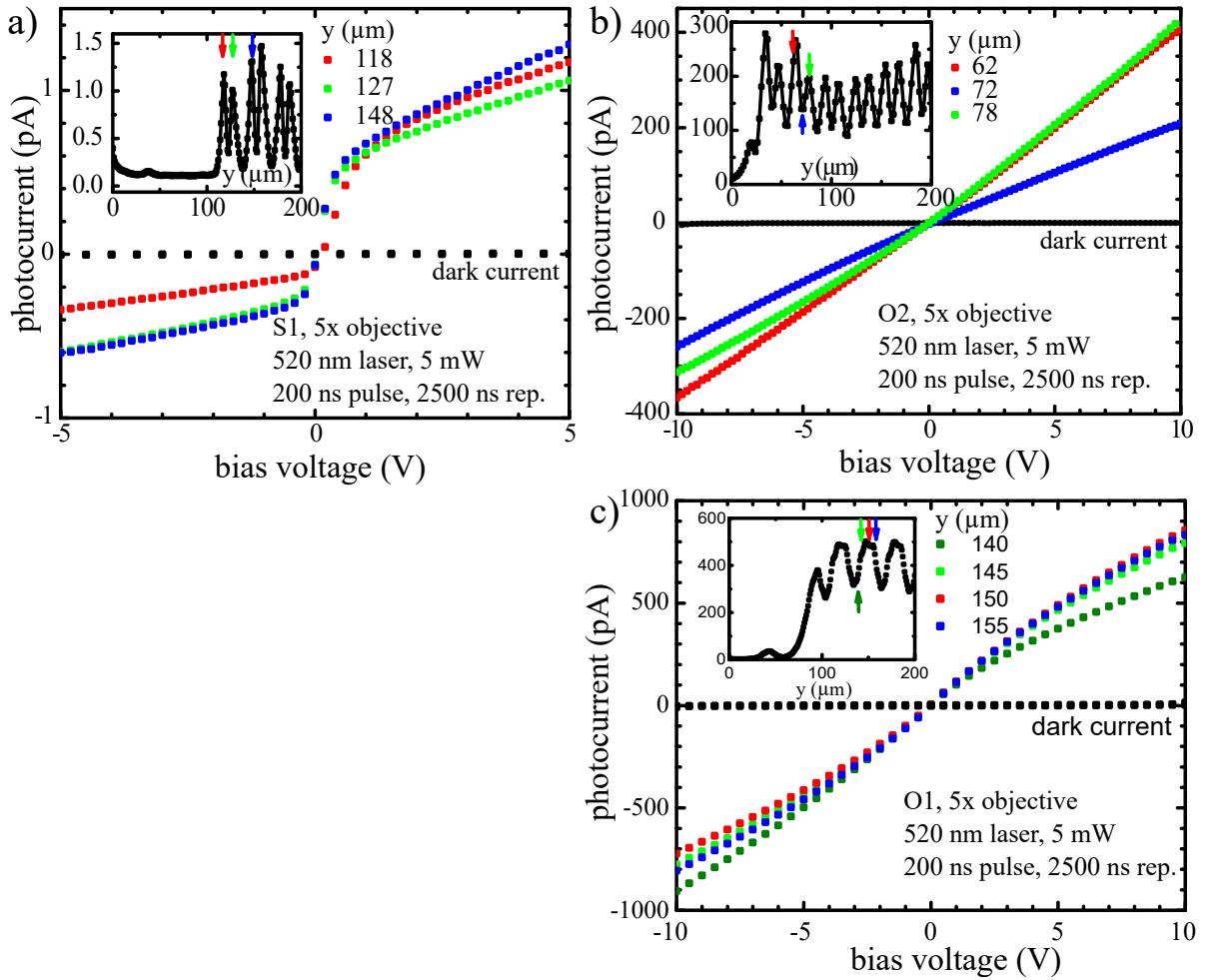


Figure 3.3: a) Data of the back-to-back U-I characteristics for sample S1 and b), c) an approximately linear behaviour for ohmic samples O2 and O1. The insets show photocurrent scans across the samples in a direction perpendicular to the interdigital contacts (y).

tic.

Photocurrent

A 5x objective homogeneously illuminates a diamond volume between several metal contacts. Photoabsorption creates mobile charge carriers in the valence and conduction band that are separated locally by an electric field, when a bias voltage is applied. The mobile charge carriers get then accelerated to the corresponding metal contacts giving rise to the photocurrent measured by the TIA. Results are shown in Fig. 3.3.

For S1 a classical back-to-back diode characteristic is observed. Depending on the bias

voltage sign either the first or the second Schottky contact is reverse biased, effectively limiting the total current. All three curves for S1 under illumination were taken on photocurrent maximums which will be identified as measurement positions, where charge carrier collection is most efficient, as discussed in section 5.2.3. The slope at the origin and maximal absolute amplitude vary as a function of the laser spot position relative to the contact and the contact quality itself. For constant contact properties throughout the contact structure and for a centered symmetric illumination a point symmetric shape is expected. The physics predicts the current to follow [16]

$$I = I_s \left(\exp\left(\frac{qU_b}{nkT}\right) - 1 \right). \quad (3.1)$$

A saturation current I_s is expected for very high reverse bias voltage. However such a saturation is not observed here, since even for $U_b > 1$ V the current increases still significantly. For further analysis of this increase the device geometry and the laser beam profile have to be taken into consideration, but this will not be discussed in this work.

Sample O1's U - I characteristic (Fig. 3.3 b)) varies linearly with U_b in first approximation. A decrease in slope for $U_b < 5$ V could be attributed to effects of inhomogeneous illumination. Such an ohmic behaviour is observed for sample O2 as well (Fig. 3.3 c)). Here, the illumination spot is broader, about $15 \mu\text{m}$, as can be estimated from the y -scan across metal contacts in the inset. Focusing only on one sign of U_b , a linear dependence with a slope related to the next positive contact's properties describes the data, as indicated by the straight lines. To conclude, the U - I characteristic reveals the Schottky contact nature of sample S1 in contrast to approximately linear behaviours of O1 and O2. The total current amplitude is about two to three orders of magnitude higher for the ohmic samples.

Chapter 4

Experimental Setup for pEDMR and ODMR Detection of NV⁻ Centers in Diamond

The experimental setup will be described in this section. All elements of the entire experiment are mounted on an optical table, while most of the measurement equipment is located on a rack next to the table. Optical and microwave excitation can be controlled on a nanosecond timescale, while the implemented optical and electrical readout is averaging over hundreds of pulse sequences. The setup has been specially designed for NV⁻ center spectroscopy applications. It allows for nanometer resolution mapping of NV⁻ center photoluminescence and photocurrent. Based on these quantities sensitive to NV⁻ center population the underlying dynamical ionization and spin transition processes can be investigated. The setup with its three main components is depicted in Fig. 4.1. The optics in the figure denoted with a) includes details on the laser excitation and detection of the specific NV⁻ center fluorescence by an avalanche photodetector (APD) is discussed in section 4.1. Another readout technique is shown in part b), where one detects photocurrent as a result of a two photon ionization of the NV⁻ center. Spin dynamics can be investigated when microwave interacts with the spin. Control parameters and details of the microwave circuit are discussed in section 4.2 along with the introduced electrical readout method using a transimpedance amplifier (TIA).

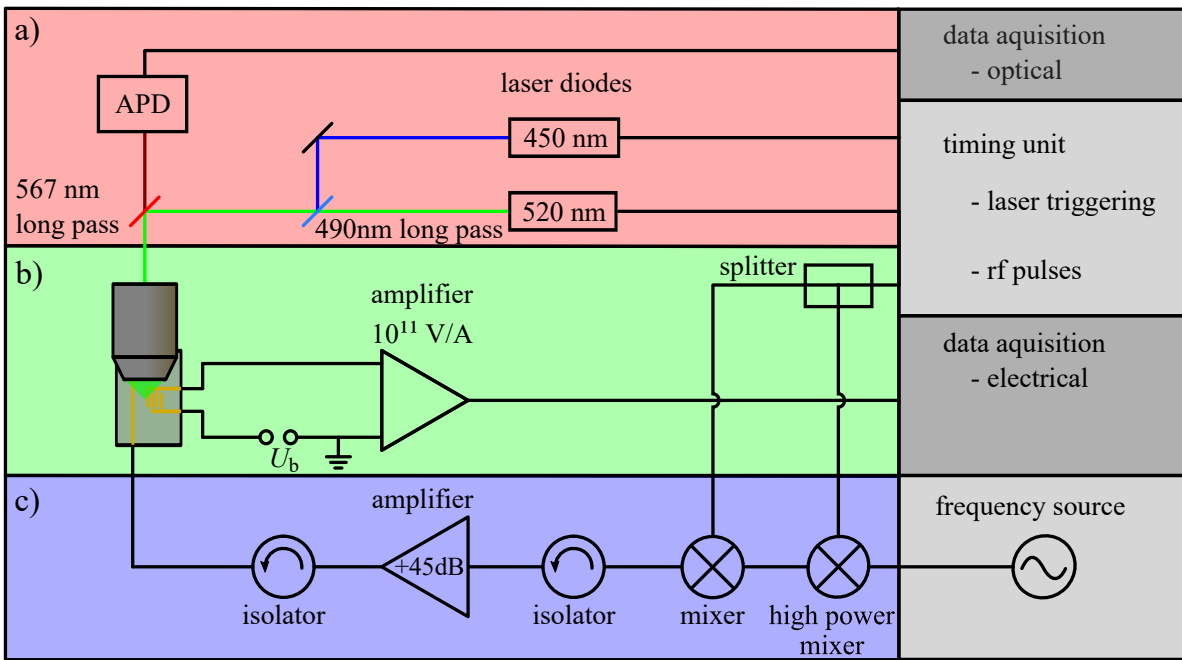


Figure 4.1: a) NV⁻ centers are excited and ionized by pulsed laser illumination, while the fluorescent light collected in the microscope objective is guided to and detected by an APD. b) Photocurrent generated in the biased MSM is converted into a voltage signal by a TIA. c) NV⁻ center spins can be driven coherently by microwave pulses provided by a massively amplified input signal originating from a frequency source.

4.1 Optics

4.1.1 Laser Sources

The optimal excitation wavelength for inducing NV⁻ center fluorescence is reported to be between 510 and 540 nm [19]. In this setup a 520 nm solid state laser is chosen, which is in the middle of this interval. In total three different lasers were included. The two other lasers beside the green laser operate at wavelengths of 450 nm and 785 nm, chosen for ionization of the NV⁰ center and NV⁻ center respectively. All lasers are in house-built systems, each based on a laser diode powered by a driver module. All laser components are depicted in Fig. 4.2, while a more detailed overview of the laser diodes is given in Tab. 4.1. For experiments with other lasers than those shown here the same optical principle can be used. For such a purpose appropriate matching of the reflection and transmission windows of the beam splitters is required.

A nanosecond pulse driver module (*picolas* LDS-VRM-05) provides laser diode currents of up to 500 mA. It can be run in continuous wave (cw) mode or in pulsed mode, where the pulse width range can be increased dynamically from nanoseconds to arbitrarily long

pulses. The laser driver itself only amplifies the input signal. A signal source sends the desired pulses of specific height and width to the picolas driver. In our case we use a 80 MHz waveform generator (*agilent* Agilent 33250A) producing pulses from 20-2000 ns length with 5 ns rise time. The signal source is triggered by the experiment's length timing control along with all other instruments like microwave source, positioning stage or detection systems. In section 4.3 the entire set of experimental steps is represented in the time domain for an exemplary pulse sequence.

An elliptical beam with different aspect ratios for different lasers is the result of an aspherical lens in front of the laser diode. Here the desired numerical aspherical lens aperture is given by the diode's beam divergence. All aspherical lenses used have anti-reflection coatings appropriate for the corresponding wavelength regime in order to reduce laser intensity losses. For a precise positioning of the aspherical lenses mechanical stages with micrometer drives were used. Adjustments of the diode-lens distance allow for collimating the laser in a controlled way.

Although the laser power does not exceed the milliwatt range, the power consumption of the laser driver is not negligible. For cooling the laser driver a base plate is mounted on an aluminum heat sink. In between the two metallic pieces a thin layer of thermal compound improves heat transport. A small fan below the heat sink increases the effective air volume per time available for cooling. Beyond the heat generated by the driver module the laser diode itself has to be considered as a heat source during lasing. When the laser diode is operated at high power it may heat up, due to limited heat transport through the diode pins. An additional path for heat transport is introduced by mounting the laser diode in a metal block with apertures for the diode pins and laser light, respectively. The metal block itself is screwed on the heat sink, separated only by an insulating mica foil and thermal compound.

The setup provides thermally stabilized lasers that can be driven at various pulse lengths, repetition rates and powers. All mentioned parameters can be controlled digitally by the experiment control program. Detailed information on the characteristics of the laser performances along with data of the laser suppression in the photon detection is provided in appendix A.

4.1.2 Confocal Microscopy

A confocal microscope uses one microscope objective for excitation and collection of fluorescence. With the microscope objective in the correct height above the sample both illumination of a small sample volume and collection of reflected or fluorescent light is possible. In general a beam splitter is necessary to couple a light source into the

laser	λ (nm)	$\Delta\lambda$ (nm)	max. power (mW)	beam divergence (°)
blue	450	2	80	11 × 25
green	520	2	50	7 × 22
NIR	785	not specified	90	9 × 16

Table 4.1: Manufacturer's specification of the laser diodes. $\Delta\lambda$ denotes the laser linewidth.

optical path from the objective to a photodetector. In this section a confocal microscope with two light sources, each coupled in with a corresponding beam splitter, is described. Investigation of multiple photon excitation with different photon energy demands high accuracy in the laser alignment, because excitation and detection of the same sample volume has to be ensured. This section discusses details on the optics of the microscope in the setup, for which a schematic overview is given in Fig. 4.2. The focus lies on the optical components required for confocal fluorescence microscopy for of one or two laser excitation.

In Fig. 4.2 b) the laser module is depicted next to the signal source. Two mirrors on kinetic mounts can be used to adjust the available degrees of freedom for a laser, position and direction. Precision screws on the mirrors allow for repeatable adjustments of the laser path. The third mirror is a dichroic long pass filter reflecting the laser light and transmitting fluorescent light to the APD. An additional mirror is mounted in such a way that it directs the incident laser light into the microscope objective. Depending on the inserted objective the focused laser spot occurs at a distance of 3.5 mm or 22 mm. The sample is glued to a sampleholder which is mounted itself with isolated clamps on a piezostage. In the large aperture of the piezostage an objective can be inserted, either with 5x¹ or 100x² magnification. Details on the objectives including the numerical aperture (*NA*) values are shown in Tab. 4.2, spot sizes are given for both axial and lateral direction.³

Coarse positioning can be performed along the *z*-axis with a micrometer screw correcting the distance of the objective to the sample holder, as indicated in Fig. 4.2 c). Feedback is provided by either the visible light being transmitted or reflected by the diamond, the NV⁻ center photoluminescence signal or the photocurrent signal. Fine tuning of the sample position is done with the piezostage, this will be described in the following paragraph. It has to be stated however, that thermal long time fluctuations cause

¹Zeiss, Plan-Neofluar 5x/0,15 Ph 1, *NA*=0.15, <https://goo.gl/hdCM1T>

²Olympus, LMPLFLN100x, *NA*=0.8, <https://goo.gl/3PqL1D>

³Diffraction limited lateral and axial spot sizes are calculated for a 520 nm laser using

$d_{xy} = 0.61\lambda/NA$ and $d_z = \lambda/(NA)^2$, respectively.

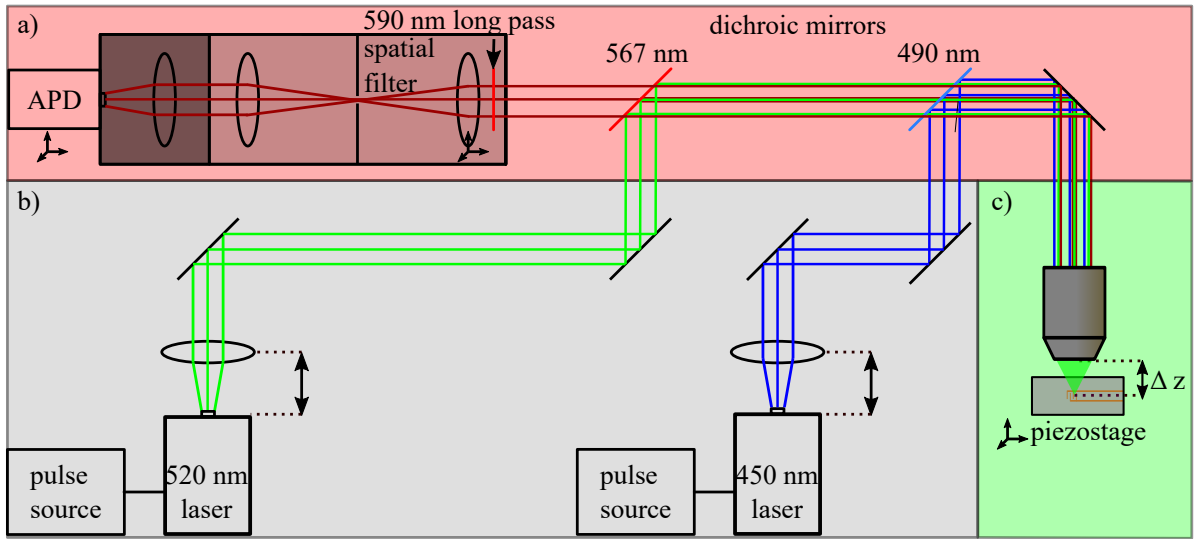


Figure 4.2: a) The optical detection system transmits mostly light from NV^- while filtering out the reflected laser light and light from NV^0 fluorescence. Better depth resolution is achieved by implementing a spatial filter. b) A pulse from the timing unit is amplified by a laser driver module. The generated light is emitted into free space and collimated by an aspherical lens, resulting in a collimated elliptical laser beam. Position and direction of laser beams can be adjusted with two mirrors, whereas additional dichroic mirrors allow superposition of two lasers differing in wavelength. c) A microscope focuses the laser down to diffraction limit. Fluorescent light from this excitation spot is collected by the same objective and guided to the APD.

mechanical stress leading to misalignment over time in the optical setup with dimensions of meters.

Calibration of the detection mechanism can be achieved in the following way: First of all a glass cover slip or mirror is mounted above the objective to generate a well defined reflection of the incident laser light. The rejected light gets collimated by the objective when the mirror is positioned in the focus plane. The laser reflex can be used to adjust the mirrors in order to superpose incident and reflected light, being an easily detectable phenomena indicating parallel beam paths. It has to be ensured that the laser illuminates the microscope objective's aperture. Further, by modulating slightly the focal distance (Δz) of the microscope objective and the sample, deviations from parallelism in the laser path occur as a xy -shift of the laser reflex with respect to the incident laser path. The convention used throughout this thesis is that z corresponds to the direction of incident laser light propagation, whereas x and y span the plane perpendicular to the z -axis. Indeed the mentioned xy -shift of the reflex can be observed visually on a screen with an aperture for the incident laser. While the spot shifts

objective	magnification	<i>NA</i>	working distance (mm)	spot size (μm)
LMPLFLN100x	100	0.8	3.5	0.4 / 0.8
Plan-Neofluar 5x	5	0.15	22	21.1 / 23.1

Table 4.2: Microscope objectives used in the NV spectrometer. The calculated lateral and axial spot size is given.

periodically with the modulation, the mirror system can be used to minimize the shift amplitude. The minimum of zero amplitude is reached when the laser beam path is parallel to the objective's axis.

4.1.3 Single Photon Avalanche Detector for NV⁻ Fluorescence Detection

Silicon as detector material is a good choice for detection of the NV⁻ fluorescence, due to its sufficient photon detection efficiency in the spectral range from 400-1000 nm. We use a single photon avalanche detector (*excelitas* SPCM-AQRH-10) with a photon detection efficiency η meeting the requirements: In the main part of the NV⁻ fluorescence from 600-800 nm, η is above 60%, but also further utilization might be considered when photon detection in the interval of 400-1000 nm is required ($\eta > 10\%$). When it comes to detection of single photons not only a high quantum efficiency but also detector dead times and dark counts become important. The APD is specified to perform at a dark count rate below 1500 counts per second (cps), however we determine the real value to be 600 cps. With a dead time of $\tau_d = 22$ ns after detection of a photon a rough estimate for the maximal count-rate yields $1/\tau_d \approx 45$ Mcps. And indeed, the manufacturer specifies the maximum count-rate before saturation to be 37 Mcps, close to the estimate. To describe correctly the dependence on incident count rate and measured value a correction factor is introduced. Linear behavior is guaranteed at count-rates below 1 Mcps, while correction factors of >1.4 above 10 Mcps have to be taken into account. Time resolved data acquisition could be possible using a fast readout device, allowing for detection of the decay times on a ns timescale.

For the alignment of the optical detector path the same reflected laser light may be used. The detection system as shown in Fig. 4.2 a) consists of a band-pass filter, spatial filter and a focusing lens in front of the detector chip. All mentioned components are protected from room light by a black casing. Light coming from the objective in reverse direction passes the long pass filters and enters the casing through an aperture

of about 10 mm. There is an additional filter, a long pass filter absorbing below 590 nm, suppresses remaining laser reflections and NV⁰ fluorescence. It is mounted together with a planoconvex lens on a *xyz*-stage. A spatial filter, a set of two lenses and a pin hole in the lens foci, selects one plane for transmission. Light from other sources is not focused on the pinhole, which results in massive light suppression behind the pinhole. The components used are a planoconvex lens (*thorlabs*, $f=150$ mm), a 100 μm pin-hole (*thorlabs*, P100S) and a collimating planoconvex lens after the pinhole (*thorlabs*, $f=75$ mm). Finally another lens ($f=40$ mm) projects the pinhole on the detector chip, where the fine positioning is enabled by a *xyz*-stage of the APD. Within the optical alignment it was ensured that lenses are mounted perpendicular to the light path. To observe this experimentally the 590 nm long pass filter was removed, resulting in a sufficient intensity of laser light being reflected from a glass cover slip. On this well defined axis the entire photodetection system was aligned. Special care was taken of mounting the lenses along the z -axis by centering lens reflections on the incident light path. Once lenses and pinhole were mounted, the pin hole was brought into focus by manually fine tuning the distance. Finally, for the detector positioning step incident light intensity was reduced with a neutral density (OD) filter to prevent damage due to excessive light exposure.

After this aligning process a spectrometer calibration is recommended for a quantification of the laser suppression and dark counts. An exemplary data set is shown in appendix A.3

In conclusion the used APD meets the requirements of detecting NV⁻ fluorescence counting individual photons. Combined with a spatial and a long pass filter a small fluorescing volume in the sample can be investigated.

4.2 Electronics

4.2.1 Low Noise Transimpedance Amplifier for Photocurrent Detection

The level of photocurrent is mainly dependent on

- density of NV centers,
- illumination intensity,

- bias voltage,
- repetition rate of the laser pulses and
- photoconductive gain,

as discussed in more detail in sections 2.3 and 5.2. However, under typical experimental conditions we obtained current levels in the pA regime, when the sample is biased. If not stated otherwise, the bias voltage is 5 V, provided by a stable voltage source (*Yokogawa GS200*). A low noise TIA (*femto DDPICA 300*) is capable of realizing amplifications up to 10^{11} V/A at a bandwidth of 20 Hz and up to 10^{13} V/A in slower operation modes. The amplified signal at the TIA output is read out by a multimeter (*Keithley 2000*, 6 1/2 digits). Optimizing parameters for the readout considering a measurement delay corresponding to the TIA rise time and the integration time allows low noise current detection comparable to the TIA specifications.⁴

4.2.2 Microwave Circuit

Electron spin resonance in the NV⁻ center is performed with strong mw pulses applied on a gold wire in close vicinity of the illuminated sample volume. An initial rectangular pulse is split equally in two parts by a power splitter (*minicircuits ZAPD-4+*), as shown in Fig. 4.1 c). One pulse fraction is mixed with a carrier frequency of 2-3 GHz in a frequency mixer (*minicircuits ZX05-43-H+-ST*). The local oscillator input is fed by a frequency source (*agilent E8257D*) signal of 13 dBm. Subsequently a second frequency mixer (*minicircuits ZX05-43-H+-ST*) optimizes the mw pulse shape by multiplying it with the initial pulse. Both frequency mixers are passive elements, absorbing a fraction of the input power, typically 6 dB. After the desired mw pulse has been formed it is amplified to a microwave power of 10 W. For sample S1 the microwave power at the gold wire was determined to be 9 W with a fast microwave diode. For O1 and O2 a microwave power of 14 W and 11 W was recorded. The rf amplifier (*minicircuits ZHL-16W-43+*, typ. gain +45 dB) is isolated with circulators to reduce reflections. One circulator (*mcli IS-10-1*) reduces internal amplifier reflections passing the input port, otherwise perturbing the mw mixing, whereas the second circulator (*mcli IS-10-10*) protects the amplifier output from reflections at the sample. The microwave interface

⁴Spectral input noise density of $1.3\text{fA}/\sqrt{\text{Hz}}$ for the $10^{10} - 10^{11}$ V/A and $0.2\text{fA}/\sqrt{\text{Hz}}$ for the $10^{12} - 10^{13}$ V/A amplification regime.

at the sampleholder is given by SMA-connectors. Finally, the microwave terminates in a 50Ω resistor at the end of the sampleholder's transmission line which absorbs most of the mw power.

Analysis of the power levels at the mw components reveals the following: The initial local oscillator signal of 13 dBm gets mixed with the rectangular pulse at the rf port, resulting in a mw output power of 7 dBm because it is attenuated in the first mixer by 6 dB. After the second mixer with the same attenuation of 6 dB the pulse power is about 1 dBm. Considering both circulators also as damping elements one ends up with a +45 dB amplification of rf pulses to powers of about 45 dBm, or 30 W. This relates to a rf power of 10-20 W, as determined by an independent measurement with a mw diode.

4.3 Timing Control

Operating coherently with an ensemble of quantum states requires precise control of the excitation. To obtain a better understanding of the underlying dynamic processes an experiment requires a time resolution better than the time constants given by the system under study. For the NV⁻ center in diamond it is known that spin dependent lifetime of the optically excited state is 13 ns for the triplet state or 77 ns for the singlet state, as introduced in section 2.1.2. It is obvious that any experiment allowing for a study of the dynamics in the NV⁻ center has to operate on a timescale comparable to the lifetime of states. Further it turns out in theory and experiment that singlet triplet transition Rabi times τ_R under the given microwave powers are in the order of 100 ns. Optimization of microwave pulses makes only sense, when the length can be varied by few percentages of τ_R . The choice of a pulse card with a 500 MHz clock used for timing control meets the mentioned requirements, both for optical induced electron transitions and microwave induced transitions of the spin system. On multiple channels pulses of variable length and spacing can be programmed with 2 ns resolution. The following section 4.3 describes how the excitation pulses evolve within the setup.

Excitation Pulse Sequence

The pulse card (*spintronics* PBESR-PRO-500) is capable of producing pulses as short as 12 ns with a 2 ns resolution. The time resolution is a consequence of the clock frequency of 500 MHz, while the shortest pulse duration is given by internal electrical circuitry. Typically two pulses from the timing unit control the excitation, one pulse restricting the length of the microwave pulse (p_{MW}) and a second pulse acting as trigger for the

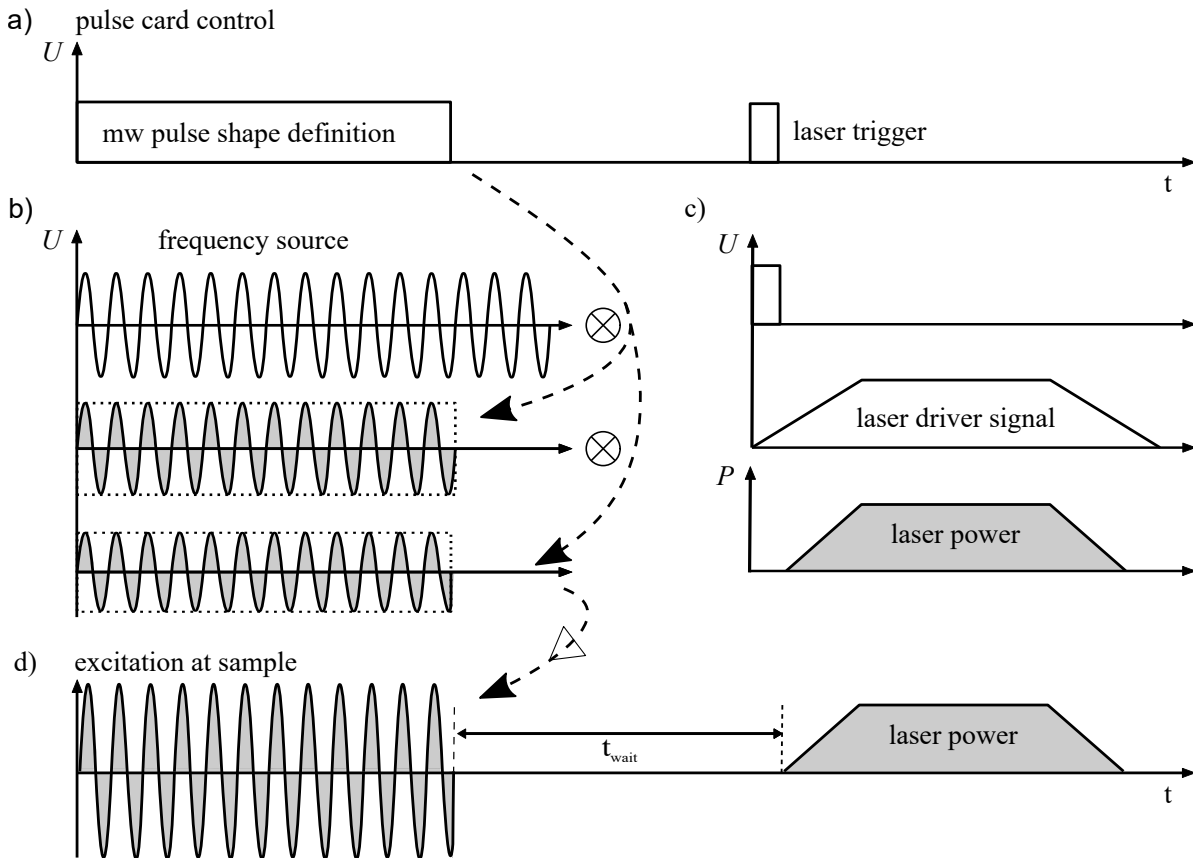


Figure 4.3: A pulse card coordinates the optical and microwave excitation of NV⁻ centers. a) A control pulse defining the width of the microwave excitation and a laser trigger pulse are generated. b) Composition of the microwave pulse by mixing twice p_{MW} with the desired frequency. c) Additionally a pulsed signal source triggered by another control pulse operates the laser driver. d) Both the length of the pulse sequence and the reference times between pulses can be adjusted as required.

laser signal source. Both pulses can be launched with adjustable reference time. How these pulses evolve during the experiment is illustrated schematically in Fig. 4.3. A first mixer composes a signal from the frequency source with a 50 % fraction of microwave pulse power. A second mixer optimized for lower powers again mixes the resulting signal with the other part of the initial rectangular pulse. Both mixers effectively suppress the microwave power leak through to the sample when no pulse from the timing unit is applied. The strong excitation mw field is generated by a subsequent amplification, as illustrated in Fig. 4.3 b).

In Fig. 4.3 c) the laser pulse generation with respect to the control pulse is depicted. An initial TTL pulse is released by the pulse card triggering the signal source to form a rectangular pulse of required length and amplitude. At next the laser driver translates

this signal into a laser pulse, details of this conversion are discussed in appendix A. The pulse card generates pulses of up to 24 distinct outputs, where currently the first three are assigned to the lasers and the fourth to the microwave circuit. In the control program the required parameters for the timing unit can be set arbitrarily in the limits of 2 ns resolution and a minimal pulse length or pulse delay of 12 ns, spacing of pulses requires a definition of a reference time. Available reference points may be chosen at the end or start of the subsequent pulse. It might be necessary to check pulse delay differences directly at the sample caused by different cable lengths or instrument reaction times, especially when small time delays of several ns play a nonnegligible role.

Chapter 5

Basic Experiments

In this chapter the experimental investigation of the NV⁻ center is presented. First of all the optical excitation with laser light followed by optical and electrical detection is presented and how the device performs under laboratory conditions. Two detection techniques, electrical and optical detection of magnetic resonance (EDMR and ODMR, respectively), are presented separately, to be used interchangeably later on. When the basic signal generation principles are understood the experiment can be extended to study spin-microwave interactions in detail (sections 5.1.2 and 5.3). Characteristic experiments demonstrating spin control are shown in section 5.3 including a discussion of electrically and optically detected magnetic resonance results. Improvement of spin contrast is conducted by investigating the dynamics of NV⁻ center ionization in chapter 6.

5.1 Photoluminescence Detection and ODMR of NV⁻ Centers

The photoluminescence intensity strongly varies with the choice of the microscope objective. The benefit of high spatial resolution and high optical power can be realized with the 100x objective, a much more homogeneous illumination in the detection volume is achieved when the 5x objective is used. Depending on the application the objective meeting the requirements best is chosen. First the resolution of laser excitation and the detection method will be discussed in section 5.1.1. With this background information on the illumination conditions ODMR results can be interpreted better (section 5.1.2).

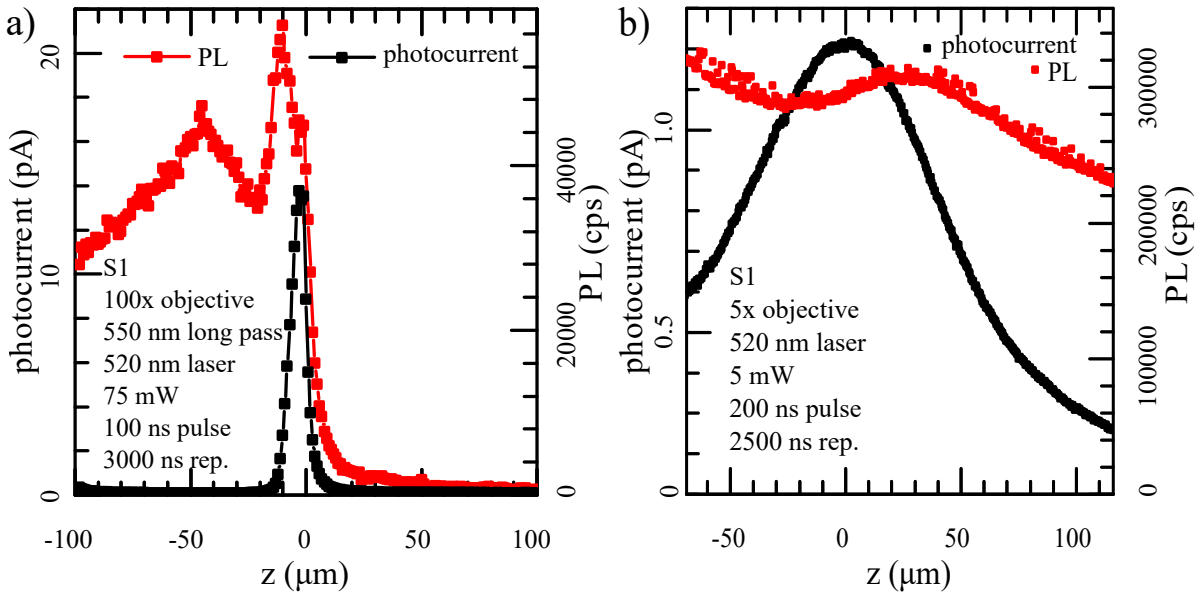


Figure 5.1: a) When the diamond surface is brought in focus a steep increase in photocurrent (black data points) is observed. Carrier transport is optimal close to the surface resulting in a decrease as the laser penetrates the sample. The situation is different for the photoluminescence (red), where photons emitted by excited NV^- centers penetrate the transparent sample regardless of the excitation depth. b) Homogeneous illumination of a small sample volume with a 5x objective. A lower spatial resolution is the trade-off.

5.1.1 Spatial Resolution of the Photoluminescence Detection

The maximal resolution utilizing the objective with 100x magnification can be achieved when the sample surface is brought into focus. Strong 520 nm laser pulses of 50 mW ionize the NV^- centers in a two photon absorption process. The incident elliptical laser beam is focused down to a spot limited by the width of the point spread function (PSF), which is determined by the beam profile and the objective's NA [29]. The resulting signal as it is measured by the optical detection system is the convolution integral of the light profile with the laser intensity-dependent photoluminescence and the spatial transmittance of the detection system. Only photoluminescence photons emitted in the excitation plane are projected on the detector chip as a consequence of the spatial filter selection. Exemplary data for a high resolution scan in axial direction is shown in Fig. 5.1 a).

In the data set the z -axis origin is set to the sample surface. How the surface position is identified by using analysing the photocurrent is explained in section 5.2. Theoretically a diffraction limited axial spot length of $1.1 \mu\text{m}$ is expected for a Gaussian beam profile of the 100x objective. However, for positive z , where the laser spot is above the surface,

still PL intensity is detected due to an out-smearing of the focused laser spot. This effect increases with larger, non Gaussian beam diameters and thus also increases for elliptical beams with aspect ratio >1 . When the spot hits exactly the surface the detected APD signal is maximal, most probably due to imperfect suppression of reflected laser light. A setup characterisation regarding this effect is attached in appendix A.3. A more or less constant PL intensity is observed when the focus is in the sample volume, in good agreement with an uniformly nitrogen-doped diamond sample with homogeneous NV⁻ center concentration. Remaining z dependencies can be attributed to shading of fluorescent diamond material by metallic contacts, as the diameter of the illuminated surface reaches the contact gap size. The lateral resolution of the confocal microscope will be discussed in section 6.1.1 in more detail.

When homogeneous illumination is required, a laser spot of dimensions larger than the volume of interest has to be generated. With a 5x objective a laser spot size of at least 23 μm axial length and 21 μm width is created, in good approximation homogeneously illuminating the uppermost conductive diamond layer.¹ The photoluminescence data in Fig. 5.1 b) shows a pronounced first maximum at $z \approx 25 \mu\text{m}$ followed by a decrease in a depth of about -20 μm and rising to the original maximum value for $z < -50 \mu\text{m}$. Again, the variation can be explained by shading of illuminated volume by a single metal contact. Compared to the objective with higher resolution, the out-smearing of the PL signal is much more pronounced.

5.1.2 ODMR on NV⁻ Centers

The spin of the NV⁻ center can be addressed with microwave pulses. Here, investigation of the photoluminescence as a function of microwave frequency, commonly called an ODMR experiment, will be discussed as a readout technique. It is known, that the spin polarization of NV⁻ centers can reach 80 % under cw laser excitation even at room temperature [30]. To study spin dynamics pulsed laser and microwave sequences are used, where the APD integrates photoluminescence over many cycles. Rectangular microwave pulses of variable frequency are used to manipulate the spin by inducing transitions from the ground state singlet $|1\rangle$ to the doublet $|2\rangle$, expressed in the nomenclature of section 2.1.2. The photoluminescence change induced by spin preparation before laser excitation will be discussed in this section. In absence of microwaves electrons get excited and relax into the NV⁻ ground state, symbolically written as $|1\rangle \rightleftharpoons |3\rangle$. The nonradiative relaxation into the dark state, $|3\rangle \rightarrow |5\rangle$, can be neglected since the

¹These values for the spot size were calculated for a Gaussian beam profile and an objective with $NA=0.15$, see section 4.1.2

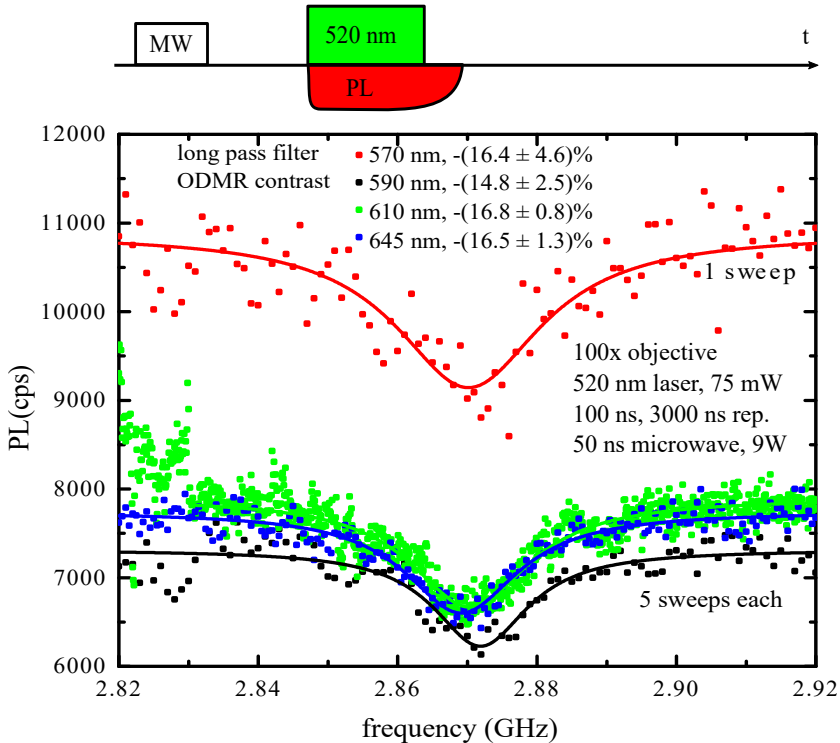


Figure 5.2: Under green laser illumination microwave driven spin transitions lead to the population of the non-fluorescent dark state, detectable as a decrease of PL. The ODMR data were measured using different filters in the APD detection system. Solid lines are Lorentzian fits to the data. For the 610 nm filter measurement the first off-resonance data points were recorded with the laser in a cold state and therefore excluded from the fit starting at 2.83 GHz. This signature did not reappear in sweeps 2-5, indicating a switch-on effect. (top) The applied pulse sequence is shown schematically, not to scale in time or intensity.

partial lifetime $\tau_{31} \ll \tau_{35}$. When the NV^- spin is initialized into $|2\rangle$ the excited electron undergoes the laser-induced transition $|2\rangle \rightarrow |4\rangle$. Nonradiative relaxation here is important, since the transition rate to the dark state is comparable to the radiative decay rate, $\tau_{42} \approx \tau_{45}$. The resulting population of $|4\rangle$ is lowered by the fraction of electrons being stored in the dark state, which is close to zero for initial state $|1\rangle$ and significantly large for initial state $|2\rangle$.

Photoluminescence is measured during a continuously repeated pulse sequence. A 50 ns microwave pulse of 9 W acts on all NV^- centers in the sample. Due to different strengths of the radially decreasing electromagnetic field spin transition efficiency varies with the distance from the microwave wire. Depending on duration, strength and frequency of the interaction with the electromagnetic field forms a superposition of states $|1\rangle$ and $|2\rangle$.

A strong 520 nm laser pulse of 100 ns duration excites a diamond volume in focus of the high magnification objective. The laser excitation is delayed by 100-200 ns with respect to the end of the microwave excitation pulse to ensure well defined experimental conditions. Spin coherence outlasts this delay by far since both spin coherence and relaxation times are much longer than this delay. Spin coherence time depends strongly on nuclear and paramagnetic impurities, where ¹³C is the dominant decoherence source in type IIa diamonds [31]. Ensemble NV⁻ spin coherence times exceeding hundreds of μ s even at room temperature have been reported for comparable type IIa SCD substrates. The signature of the NV⁻ center spins undergoing transitions into |2> can be seen in the experimental data as a signal reduction at a frequency of 2.87 GHz, where the microwave photon energy $E_{\text{MW}} = hf$ matches the zero field splitting parameter $D = 0.012$ meV. As used in the following section 5.2 the signal reduction, always measured relative to the off-resonant total amplitude, is called contrast. The signal-to-noise ratio of 20:1 can be improved by increasing the photon count rate and waiting for the laser to stabilize after switch on. A Lorentzian is fitted to the data describing an absorptive process. From the fit the parameters linewidth, resonance frequency and amplitude of the resonance can be obtained, yielding an ODMR contrast of -(15 ± 2) %. This experiment was repeated with different PL filters in order to find optimal experimental conditions providing maximal spin contrast.

Selecting an Appropriate PL Filter

If there were other photoluminescent sources than NV⁻ centers long pass filters are the instrument of choice for reduction of PL that is not attributed to the NV⁻ center. One would expect a cutoff wavelength close to the NV⁻ ZPL to show best performance. The very same ODMR experiment from above was conducted after changing the long pass filter in the photodetection system to different ones with cutoff wavelength at 590 nm, 610 nm and 645 nm, respectively. The optical path was readjusted after every filter change to exactly map the excitation spot to the detector. Experimental results are shown in Fig. 5.2.

A major difference is the difference in total signal amplitude, being at a similar level for all filters but the 570 nm filter. This can be attributed to a weak suppression of reflected laser light by this filter. Since laser reflection is not influenced by the microwave field it just gives a constant contribution to the PL signal. Without the reflection offset, that can be suppressed with other filters, ODMR contrast is theoretically higher. In an independent experiment the suppression quality of the detector system with the 590 nm long pass filter has been characterized. The intensity of 520 nm laser light reflected

from a mirror was measured with the APD system for different incident laser powers (appendix A.3). From these measurements we can conclude, that still laser light enters the detection system, but an upper limit of this parasitic effect can be evaluated.

Taking a closer look at the noise level reveals highest fluctuation for the 570 nm data set. The other curves are the normalized result of five similar frequency-sweeps conducted in sequence. Lorentzian fits provide the area of the resonance and line width, from which the contrast can be derived. The independent errors of line width and dip area determine the contrast errors according to the rules of error calculation. We note the small shifts of about 1 MHz from resonance frequency 2.871 GHz within in the data sets, that can be explained by uncertainties originating from the low signal-to-noise ratio in this measurement. For data analysis the comparatively low dark-count rate of 600 cps was not subtracted. Within the error bars contrasts of all data sets coincide with an ODMR contrast of 16%. Without any significant difference between filters 590, 610 and 645 nm we decide for 590 nm, because its relatively low cutoff wavelength provides full transmission of the NV⁻ PL spectrum.

5.2 Photocurrent Detection

So far we focused on the PL signal for detecting the spin resonance. In this section the pEDMR method will be explained and demonstrated in detail. The first aspect is finding the right power range for pEDMR, then spin transition experiments will be shown. Even in the absence of an external magnetic field the spin of the NV⁻ center is oriented along the NV⁻ center axis. The ground state reveals a fine structure, a prerequisite for Rabi experiments that can be used for investigation of spin transitions in a two level system (section 5.3.1). Having learned about the microwave spin initialization further insight into photocurrent dynamics is obtained from a detailed study of laser excitation time and intensity. Optimal spin contrast is obtained for a laser pulse length that relates to internal transition times of the NV⁻ center.

5.2.1 Two Photon Ionization of the NV⁻ Center

For photoionization in diamond more than one visible photon is required. In the model introduced in section 2.1.3 a four photon process is described for green laser light. Experimentally access to this multiple particle excitation is provided by an analysis of the laser power-dependent photoionization. Basically a rate equation system including all power-dependent NV⁻ center-related transitions has to be solved. In a very simplistic view the exponent of the power dependence equals the amount of photons involved, but

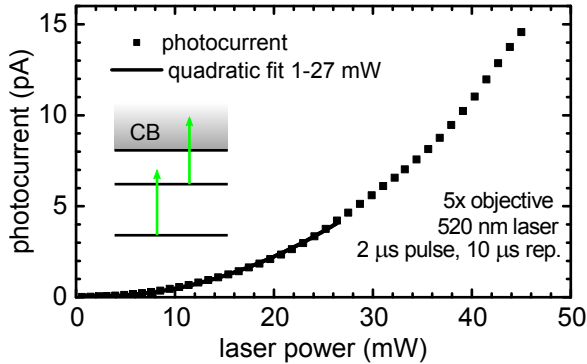


Figure 5.3: Quadratic dependence of the photocurrent for a two photon ionization process of the NV^- center. For laser powers above 100 mW the first transition saturates and the power dependence is expected to become linear [12].

this is no longer valid in the presence of saturation effects. If population inversion occurs, higher laser power does not result in more photoexcitation since there are no more electrons available for excitation. The experiment was conducted on sample S1 under homogeneous laser illumination with the 5x objective. The main feature in the data observed, shown in Fig. 5.3, is a quadratic laser power dependence of photocurrent. Two transitions determine the observed quadratic relation, transition $|\text{1}\rangle, |\text{2}\rangle \rightarrow |\text{3}\rangle, |\text{4}\rangle$ from NV^- ground state to its excited state and subsequent $|\text{3}\rangle, |\text{4}\rangle \rightarrow \text{CB}$. Recharging NV^0 to NV^- by photoexcitation of NV centers with an electron from the valence band is thought to take place on a timescale much faster than NV^- center ionization [22]. The dark state does not provide a parallel competing ionization path and can be interpreted as a reservoir for a very small fraction of electrons that do not relax into the optical ground state. From the dark state electrons relax through another dark state level back into the ground state. The relaxation process from the dark state into $|\text{1}\rangle$ or $|\text{2}\rangle$ can be described by two time constants 289 ns and 463 ns, respectively [18]. The photoionization experiment should be ideally conducted under cw laser illumination. Since pumping power is higher in pulsed mode we choose as trade-off a pulse length of 2 μs , about an order of magnitude longer than any dominant relaxation time of the NV^- center.

At low laser powers a linear contribution from N_s^0 photoionization competes with the quadratic two photon ionization contribution of NV^- centers, as reported by Bourgeois [11]. In our experiment a linear contribution is not observed, due to a substitutional nitrogen concentration in our samples that is lower by a factor 200 compared to those samples used by Bourgeois. However, with increasing laser power N_s^0 ionization is outperformed by NV^- ionization. At some threshold power population inversion of the optical ground state and excited state occurs. Further linear photocurrent increase is expected and experimentally demonstrated to occur for laser powers above 80 mW using a 5x objective ($NA=0.15$) [12]. The quadratic fit does not include data points above 27 mW to be independent of population inversion effects at higher powers. In

section 5.3.2 we will analyse which pumping power is suitable for efficient electrical NV⁻ spin readout.

5.2.2 Characteristics of the MSM Photodetector

Typically a bias voltage of $U_b = 5$ V is sufficient to accelerate the mobile charge carriers created by photoionization. The chosen U_b corresponds to an average electric field of $E = 5 \cdot 10^3$ V/cm in the 10 μm gap between contacts. The electric potential of such an interdigital contact structure is simulated with isolated metal contacts on a material with the dielectric constant of diamond. Screening effects induced by photoionized charge carriers are not implemented in the simulation. The problem can be described in two dimensions for a contact length being much larger than the width and spacing. The result for the simulated electrostatic potential is illustrated in Fig. 5.4 a).

The only 0.1 μm thin contacts are depicted as black bars for better visibility. Every second contact is connected to U_b , all others are grounded. Shown in detail is the region close to the first contact and how potential becomes nearly homogeneous 20 μm away from the contacts, which is twice the contact spacing. This homogeneity is a first indication for a depth-dependent limit in carrier collection efficiency. The inset depicts a very regular pattern for all simulated contacts that occurs close to the surface. The periodicity of 30 $\mu\text{m} = 2 \cdot (10 \mu\text{m} + 5 \mu\text{m})$ relates to that of the contact structure, when only every second, positively biased, contact is counted.

Figure 5.4 b) shows the corresponding electric field distribution for the MSM detector. Maximal field occurs at the contact edges where curvature is maximal. At the very first contact a smaller electric field can be seen from both the blurring and the lower potential difference to the unconnected area. Indeed the high field area at the first contact at $y=0$ is reduced compared to the inner contacts. Within a depth of one micrometer there is no significant change in potential and field distribution for the active, illuminated detector volume. For deeper regions, $-5 \mu\text{m} < z < -1 \mu\text{m}$, carriers have to take increasingly longer paths along the electric field lines to the contacts. Increased path length along with reduced electric field amplitude reduces the carrier detection efficiency. For $z = -7 \mu\text{m}$ the path length is twice that of a near-surface path. We can compare this value with the result of the depth-dependent scan of photocurrent with a full width at half maximum (FWHM) of 8 μm (Fig. 5.1 a)). This match confirms the argumentation from above. The photocurrent-signal observed in Fig. 5.1 a) then allows to set the diamond surface position to the higher z -value that corresponds to a half maximum value of the photocurrent. When the 5x objective is used as in

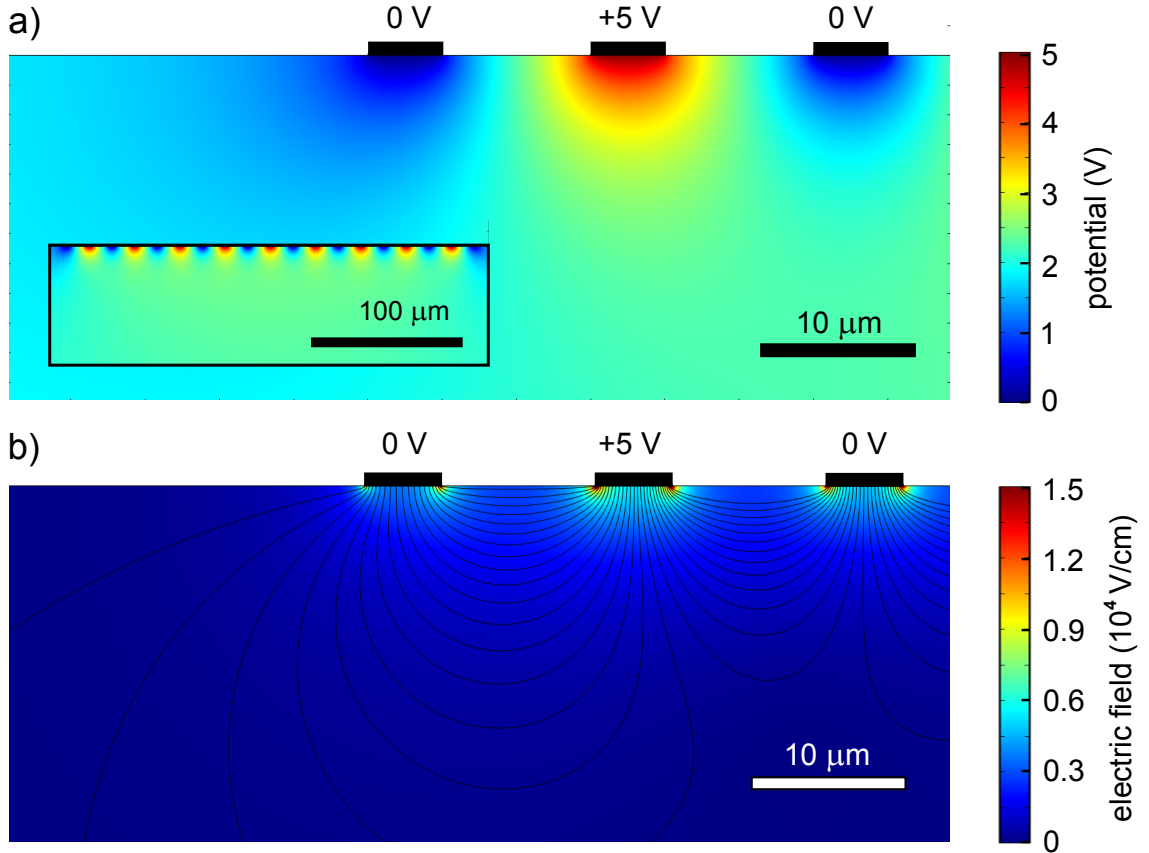


Figure 5.4: a) *Simulation of the electrostatic potential for the MSM device under 5 V bias voltage for isolated contacts. Screening of electrical field by charge carriers is not implemented in the simulation. The gap between contacts is 10 μm , the contacts are 5 μm broad and 0.1 μm thick. The inset depicts the potential periodicity of 30 μm .* b) *The electrical field is maximal in the vicinity of contacts, field-lines are illustrated as black lines and the corresponding magnitude is encoded in the background color. For carriers deeper than 15 μm collection efficiency is low.*

Fig. 5.1 b), where the photocurrent-peak is significantly broader, we set $z = 0 \mu\text{m}$ at the z -position corresponding to maximal photocurrent, neglecting the small effect that the detection of photocurrent is not perfectly symmetric to the surface. To conclude, the MSM photodetector detects charge carriers generated in an active volume close to the surface. Together with the picture of low field mobility transport (section 2.3) the working principle of the device is well understood.

5.2.3 Mapping the Photocurrent

With background knowledge on MSM detector performance and the underlying photocurrent generation process the lateral dependence of the signal will be discussed. As it will turn out it is not uniform at the surface, but the observed variations allow to select a detection volume with high signal output. Further, conclusions on the lateral resolution and the laser spot size can be drawn. Detailed diamond surface scans with the 100x objective yield data like that depicted in Fig. 5.5 a).

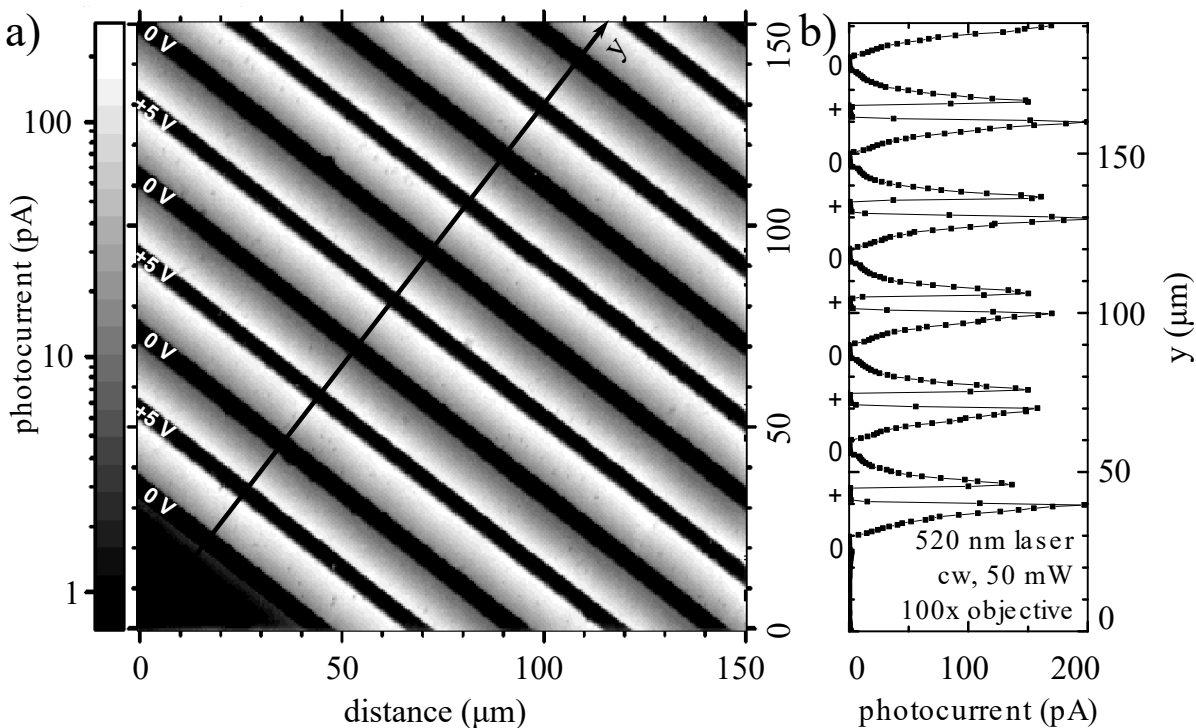


Figure 5.5: a) A photocurrent scan reveals the position of metal contacts, visible as black stripes. For better contrast a logarithmic scale is chosen in the image. In the bottom left corner charge carriers cannot be detected in absence of contacts. Data of a slice perpendicular to the contacts is shown in b). Alternating bias voltages at the contacts lead to suppressed or enhanced detection of the photo-ionized carriers.

The most prominent feature in this non-linear graphical representation are the black and white areas indicating positions of metal contacts and active detection volume. The interdigital contacts are seen under an angle of 38° with respect to the scan direction. In all experiments we assign the y -axis perpendicular to the contacts, as indicated in the figure. The x -axis completes the system of y -axis and the surface normal z -axis to a right-handed coordinate system. The data trace along the depicted line (Fig. 5.5 b)) begins at zero photocurrent at the edge of the MSM structure and continues with a reg-

ular data structure beginning at $y=30 \mu\text{m}$. As we would have expected from the electric potential simulation indeed a regular pattern with $30 \mu\text{m}$ periodicity can be observed and the contacts with $U_b = +5V$ can be identified, the first one at $40\text{-}45 \mu\text{m}$. Looking carefully to the first grounded contact at $y = 25\text{-}30 \mu\text{m}$ brings a very small photocurrent for $y < 25 \mu\text{m}$ to our focus, better visible in the logarithmic image representation. Since this is a low potential contact not electrons but holes contribute dominantly to the photocurrent. The field distribution here is very different from the homogeneous one in the area between contacts, decreasing approximately radially at this outer edge. In any gap between contacts there is maximal photocurrent detected at the positively biased side. At the first sight this is contradictory to the electric field symmetry. The interpretation here is that both holes as electrons get collected with the same efficiency close to the corresponding contact with highest efficiency, but later result in a photocurrent that is enhanced by the photoconductive gain factor.

Another parameter that can be analysed is the flank slope at the positive contacts. It is the convolution integral of the laser spot point spread function (PSF), the NV^- density and the space dependent efficiency of the MSM detector. The NV^- density is homogeneous throughout the sample but some regions shaded by the contacts must not contribute to the integral. Under the assumption of a step function modulating the NV^- density and a constant efficiency close to the contact the lateral laser PSF can be measured. For a gaussian beam profile with standard deviation σ the maximal flank slope can be determined analytically to be $\frac{1}{\sqrt{2\pi}\sigma}$.

However, since the photocurrent depends quadratically on the laser power and thus the PSF, we have only experimental access to the squared PSF, which is sharper. To introduce an easily accessible quantity one can determine the 10 % - 90 % width at a contact edge as an estimate for the spot size, for which the theoretical value is 2.6σ . From the data of Fig. 5.5 we measure $(1 \pm 0.3) \mu\text{m}$ at the sharp flanks. Further the other broader flanks can be analyzed allowing for conclusions on the MSM detection efficiency. It cannot be determined with higher precision than the spot size. The efficiency seems to decrease somehow reciprocal with the contact distance, suggesting that a detailed analysis and comparison with the field simulation have to be conducted. Another remarkable feature is a reduced height and FWHM at the contact side with higher y . This asymmetry is introduced by the laser beam, that was not perfectly aligned with the sample surface vector. However, a quantitative characterization of this effect assuming an angle mismatch of 1:100, roughly the experimental accuracy, could explain the observed differences of about 20 % when not only linear geometric effects such as shading but also non-linear electric field dependencies are taken into consideration. This will not be discussed in this work. We just state that the angle of incidence has a strong

effect on the maximal photocurrent amplitude.

5.3 Pulsed Electrical Detected Magnetic Resonance on NV⁻ Centers

With the knowledge about fundamentals of photocurrent generation of NV⁻ centers in diamond, a four photon excitation process under 520 nm laser illumination, photocurrent changes induced by a variation of electron and spin excitation will be analyzed in this section. Again, a small averaged pA photocurrent generated by a continuously repeated pulse sequence is the primary measurement signal. Conditions for maximal spin contrast will be presented and finally an outlook lists the effects limiting the pEDMR spin contrast.

5.3.1 Electron Spin Resonance

Basically, the same pulse sequence as for ODMR can be used for pEDMR. Microwave pulses initialize the spin ensemble into any macroscopic superposition of $|1\rangle$ and $|2\rangle$. The readout is conducted as follows: 520 nm laser photons induce transitions $|1\rangle \rightarrow |3\rangle$ and $|2\rangle \rightarrow |4\rangle$, dependent on the spin initialization. The main difference for $|3\rangle$ and $|4\rangle$ is the branching ratio r into the dark state, which reduces the signal amplitude when being occupied. Figure 5.6 shows experimental data for the expected signal reduction due to microwave-induced spin transitions. pEDMR data is shown next to ODMR data, both data traces are normalized and vertically slightly shifted. The inset visualizes the dominant detection mechanism for the resonant and off-resonant cases. The pEDMR data shown was recorded in two separate pEDMR measurements differing only in the frequency sweep direction to optimize the measurement time.² The two pEDMR resonance frequencies f_{pEDMR} resulting from Lorentzian fits of the different sweep directions differ by more than 10 standard deviations. This is the consequence of the time delay in the setup that is translated into a frequency shift. Since this effect is the same for both sweep directions except the sign building the averaged mean cancels the errors and yields $f_{\text{pEDMR}} = (2.87014 \pm 0.00007)$ GHz. This value is in agreement with the optical measurement that yields for the resonance frequency $f_{\text{ODMR}} = (2.87004 \pm 0.00004)$ GHz.

²A signal rise and fall constant occurred in the pEDMR measurement, that could not be observed in simultaneously recorded ODMR measurement. To reduce measurement time pEDMR data was recorded at a high sweep rate for different sweep directions and analyzed separately. This optimization of measurement time has the consequence that the photocurrent in the experiment is not in perfect equilibrium for every data point.

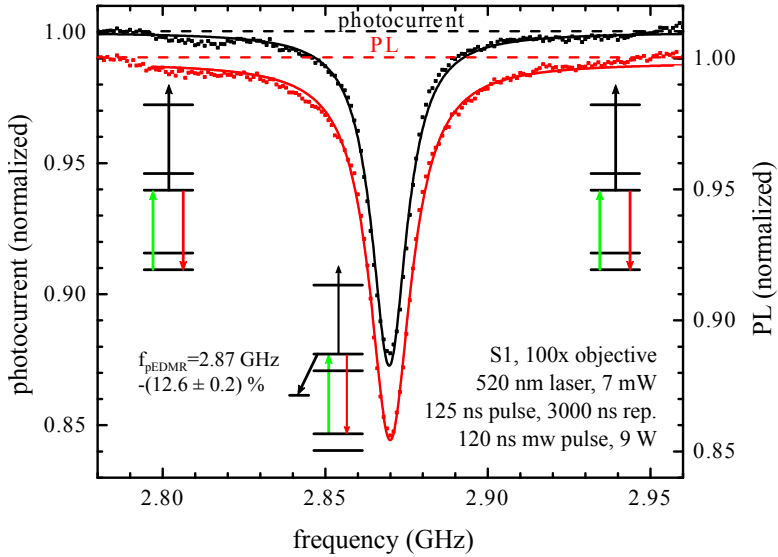


Figure 5.6: Spin resonance is observed when the microwave excitation frequency matches the zero field splitting parameter D . After photoexcitation $|4\rangle$ has a high probability to relax into the dark state, which reduces the photocurrent. For comparison simultaneously detected ODMR is shown, the solid lines are Lorentz fits.

The contrast is comparable for both readouts with a value of $-(12.6 \pm 0.2) \%$ for pEDMR and $-(14.4 \pm 0.2) \%$ for ODMR. The ODMR resonance linewidth is by 12 % broader than the pEDMR linewidth with $\text{FWHM}_{\text{pEDMR}} = (13.3 \pm 0.2) \text{ MHz}$. Basically the linewidth should be the same for both detection principles, as has been already demonstrated by [11]. Narrowing of the linewidth under higher optical power has been reported, an effect explained by a change of the longitudinal versus transverse spin relaxation time [32]. A larger FWHM for ODMR indicates then an additional signal contribution from a larger detection volume with a corresponding weaker optical power for ODMR compared to that of the pEDMR detection region exists.

For a simple model estimating the ODMR contrast we consider NV⁻ center ionization to happen at a longer timescale than relaxation. We get different branching ratios (r) from the partial life times

$$r_{35} = \frac{\tau_3}{\tau_{35} + \tau_{31}} = 14 \% \text{, and } r_{31} = 1 - r_{35} = 86 \%$$

$$r_{45} = \frac{\tau_4}{\tau_{45} + \tau_{41}} = 50 \% \text{, and } r_{42} = 1 - r_{45} = 50 \%$$

for $|3\rangle$ and $|4\rangle$, respectively. Calculating the contrast just from the difference of these partial PL life times τ_{31} and τ_{42} yields an ODMR contrast of $\frac{86 \% - 50 \%}{86 \%} = 42 \%$. We note that this is only valid for perfect initial spin polarization and short laser pulses compared to the nonradiative dark state relaxation time. For stronger pulses the sit-

uation changes due to additional ionization and recharging effects. These are exactly the processes that have to be analyzed in the case of pEDMR. Here, the optical excited NV⁻ triplet state, |3⟩ or |4⟩, requires a second photo-absorption process for the electrical readout. The ODMR contrast can be calculated just from the population of states |3⟩ and |4⟩, while for pEDMR an additional photoexcitation of these states is required. Since this photocurrent generation mechanism is quadratic in laser power a characteristic difference to the optical readout is identified. The discussion on spin contrast will be continued in section 5.3.2 including further experimental data that coincide with the data and the Monte-Carlo simulation published recently by Hrubesch [12].

Before the discussion on maximal readout spin contrast will be continued optimal spin initialization has to be ensured. The NV⁻ center has in its ground state a spin $S=1$ and consists of state |1⟩ with $m_s=0$ and state |2⟩ with spin projection $m_s = \pm 1$, being degenerate at zero external magnetic field. The triplet sub-states |1⟩ and |2⟩ are split by $D = 0.012$ meV. At room temperature the Boltzmann distribution yields only negligible differences for |1⟩ and |2⟩ occupation since $D \ll k_B T = 25$ meV. Significant polarization is achieved as follows: Under green illumination shelving over the dark state accumulates electrons in |1⟩. Then a microwave π -pulse induces the transition |1⟩ → |2⟩ and shifts the major population into |2⟩. Conditions for the rectangular π -pulse are the right frequency $f = D/h$ and duration t_π . From (2.5) we obtain by converting ω_{nut} into the frequency ν_{nut}

$$\nu_{\text{nut}} = \frac{1}{2\pi} \frac{g\mu_B B_{\text{MW}}}{\hbar}. \quad (5.1)$$

The parameter t_π can be calculated as introduced in section 2.2 as the half of a full Rabi-cycle,

$$\tau_\pi = \frac{1}{2} \frac{1}{\nu_{\text{nut}}}. \quad (5.2)$$

Assuming a magnetic field of 1.5 mT at the NV⁻ center location one obtains $\nu_{\text{Rabi}} = 4$ MHz and thus $\tau_\pi = 125$ ns using (5.2). At this pulse length maximal population of state |2⟩ and thus maximal pEDMR contrast is expected. The dynamics of spin transitions between |1⟩ and |2⟩ can be investigated by a variation of the microwave pulse duration. The contrast increases with pulse duration as |2⟩ gets populated, which is observed as signal reduction, representative data is given in Fig. 5.7 a). A contrast can be evaluated from the data by comparing the signal amplitude of resonant and off-resonant measurements that are separated by 4-5 FWHMs from resonance.

For f_{pEDMR} the photocurrent is reduced until an absolute minimum is reached at a microwave pulse duration (t_{MW}) of $t_{\text{MW}}=120$ ns or 160 ns for the different excitation spots A and B, respectively. For longer t_{MW} the signal rises slightly again and settles at a value still more than 10 % below the signal of an off-resonantly excited system.

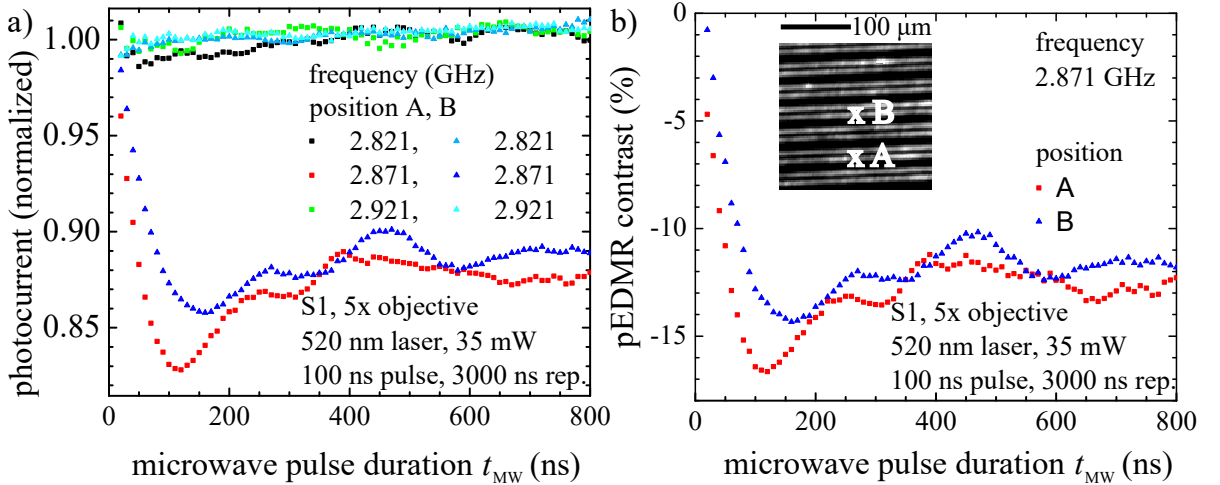


Figure 5.7: a) Microwave induced spin transition reduce the photocurrent. Minimal pEDMR signal is observed for a microwave π -pulse, towards longer times dephasing of the spin ensemble leads to a constant offset. b) pEDMR contrast varies with position since the magnetic field amplitude is in-homogeneously distributed.

With the observation of maximal contrast and thus spin polarization the corresponding microwave pulse duration can be set equal to t_π . For $t_{\text{MW}} > t_\pi$ still a t_{MW} -dependence on pEDMR contrast is apparent before saturation that is attributed to the different spin transition within the spin ensemble. NV⁻ centers are randomly distributed among four possible crystal orientations. For one of them the projection of \mathbf{B}_{MW} on the NV⁻ center axis is maximal and thus t_π minimal. Spin transition times for the other orientations are longer, depending on the alignment of \mathbf{B}_{MW} and the diamond lattice. From the data presented here a computed Fourier transformation could not provide significant results to study this effect in more detail. To conclude we end up with a maximal ensemble spin polarization after a microwave π -pulse of 120 ns at positions close to the first interdigital contact.

5.3.2 Optimization of pEDMR Dynamics

Once maximal population of state $|2\rangle$ is ensured, mainly for one of four NV⁻ center orientations in absence of an external magnetic field lifting the degeneracy of the NV⁻ orientations, investigations of the spin-to-charge conversion of our method can be conducted. In order to optimize the ionization of NV⁻ center with respect to the spin configuration different ionization laser powers (P_{ion}) and pulse duration (t_{ion}) are tested experimentally. For each data point in Fig. 5.8 b) the photocurrent signals of resonant measurements at $f_{\text{pEDMR}} = 2.871$ GHz and off-resonant measurements at $f_{1,2} = 2.82, 2.92$ GHz

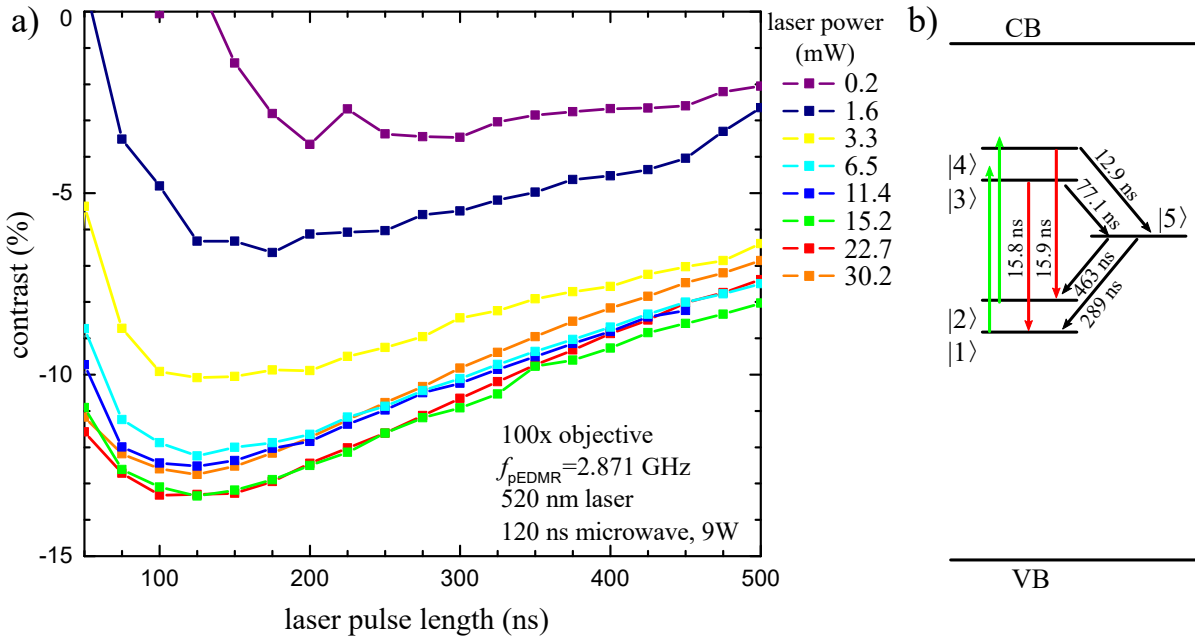


Figure 5.8: a) The contrast of the NV^- pEDMR spin readout strongly depends on the photoionization pulse. Optimal conditions can be identified and the data can be interpreted with the five state model for the NV^- center depicted in b).

were used for evaluation of the pEDMR contrast. The nominal optical power on the horizontal axis has been determined in a separate measurement. As shown in appendix A the laser power varies non-linearly with repetition time. Here, the repetition time is higher than in the calibration, leading to a small systematic deviation of a few percent for all laser intensities. The effect of pulse length has a much bigger impact since towards shorter pulse times $t_{\text{ion}} < 50 \text{ ns}$ the pulse shape deviates from a rectangle. Further, for high pulse times at high intensities heat reduced the power output of the laser. To summarize, these mentioned effects limit the determination of an accurate power and have to be interpreted as values with both statistical and nonnegligible systematic error.

Experimental errors introduced by laser intensity fluctuations were averaged out by subtracting a linear background signal. The mathematical expression used for pEDMR contrast evaluation is

$$\left(\frac{\Delta I}{I} \right)_{\text{pEDMR}} = \frac{I_{f_{\text{pEDMR}}} - \bar{I}}{\bar{I}}, \text{ where } \bar{I} = \frac{I_{f_1} + I_{f_2}}{2}. \quad (5.3)$$

The level structure as introduced in section 2.1.2 is depicted next to the data in Fig. 5.8 b). Since spin conserving optical transitions connect states $|1\rangle \rightleftharpoons |3\rangle$ and $|2\rangle \rightleftharpoons |4\rangle$ in the following discussion spin polarization refers to an generalized expression including both,

polarization of the optical ground plus that of optically excited state. For weak ionization pulses at laser power below 1 mW the contrast is quite low, being more pronounced for $t_{\text{ion}} > 200$ ns. At shorter pulse lengths the spin contrast vanishes due the decreasing contribution of NV⁻ versus N_s⁰ photoionization. A characteristic dependence describes the contrast for intermediate P_{ion} up to 6.5 mW differing only in a multiplicative constant. With rising power the spin current from |4⟩ ionization is decreased by a shelving process. The dark state |5⟩ is populated by many |2⟩ ⇌ |4⟩ transitions, where each NV⁻ excited into |4⟩ has a significant probability due to the branching ratio ∼ 0.5 to be shelved into the dark state. The same argument of increased shelving effect accounts for longer laser pulse duration, as long as relaxations from the dark state into the NV⁻ center ground states |1⟩ and |2⟩ can be neglected. With a partial lifetime of 290 ns preferably |1⟩ is populated by nonradiative dark state relaxation, effectively decreasing the system's spin polarization for t_{ion} comparable to τ_{51} . In the data a maximal spin contrast is observed at $t_{\text{ion}} = 100 - 150$ ns. For this and higher t_{ion} the |5⟩ → |1⟩ transition limits the spin contrast. The spin-dependent photocurrent generation rate is expected to go to zero for $t_{\text{ion}} > 400$ ns, which results in a lowering of the pEDMR contrast [12]. To put the performance of electrical NV⁻ center spin readout in numbers the maximal achieved contrast is -13.5 % in this experiment for $t_{\text{ion}} = 125 \pm 25$ at a 520 nm laser power of $P_{\text{ion}} = 25$ mW.

The spin selectivity of the ionization process is reduced when the average time for ionization approaches τ_{45} . Independent of the spin electrons then tend to get ionized as soon as they are excited into |3⟩ or |4⟩. The consequence for $P_{\text{ion}} > 25$ mW is a pEDMR contrast reduction for all t_{ion} and even stronger contrast reduction for long times. This effect can be verified by comparing the data sets for $P_{\text{ion}} = 22.7, 30.2$ mW, where lower contrast occurs for the high P_{ion} towards long $t_{\text{ion}} > 300$ ns. Very similar pEDMR contrast results have been obtained from experiments with more homogeneous illumination using the 5x objective, but shall not be discussed additionally here. Under the assumption that the microwave pulse did not perfectly polarize the NV⁻ spin ensemble in its initial state the presented results are in agreement with demonstration of pEDMR contrast of -16 % by Hrubesch [12]. This work additionally develops a Monte-Carlo simulation for a quantitative description of the pEDMR contrast with respect to intensity and duration of the 532 nm laser used there. The pEDMR contrast is found to be limited by nitrogen donor concentration in diamond and predicted to reach -46 % for $P_{\text{ion}} = 21$ mW in absence of substitutional nitrogen [12]. However, most recent fabrication methods for NV⁻ centers in diamond rely on irradiation processes, that do not achieve creation of a NV⁻ center for each nitrogen donor. Further, deterministic creation of single NV⁻ centers has not been realized. In a next step we will test, whether electrical spin readout

can be optimized by integration of an additional laser pulse with higher photon energy in the pEDMR pulse sequence.

Chapter 6

Dual Laser Excitation of the NV⁻ Center

Having studied and optimized the dynamics of the NV⁻ spin-to-charge conversion under 520 nm laser illumination, it was found that nitrogen donors limit the pEDMR contrast. Further contrast improvement might be achieved by separating and resolving the different excitation steps in time and by different photon energies. In section 6.1 the absence of pEDMR contrast for a purely blue laser-induced spin readout is discussed. Further findings do not indicate any contrast improvement when combining green and blue laser excitation and will be explained by a comparatively high blue laser photon energy directly ionizing the NV⁻ center ground state, regardless of its spin orientation. Another approach is to tune the photon energy (E_{ph}) for NV⁻ photoionization to prevent the parasitic N_s⁰ photocurrent contribution. A first proof of principle experiment opening the way for further investigation is discussed in section 6.2.

6.1 520 nm and 450 nm Dual Laser NV⁻ Ionization

In the first section it is shown experimentally that in diamond photocurrent generation is dominated by absorption of one photon for blue 450 nm laser excitation. In a next step a pulse sequence comparable to the green laser-driven pEDMR experiment is introduced and discussed. In a last step the assumption of direct NV⁻ ground state ionization is underlined by an experiment demonstrating reduction of pEDMR contrast.

6.1.1 Alignment of Laser Spots

The entire set of pEDMR experiments described in this chapter is performed using the 100x objective. The axial position of laser spots is determined utilizing sample S1 by z -scans close to the surface. Data of the corresponding photocurrent and PL signal is shown in Fig. 6.1 a) and b).

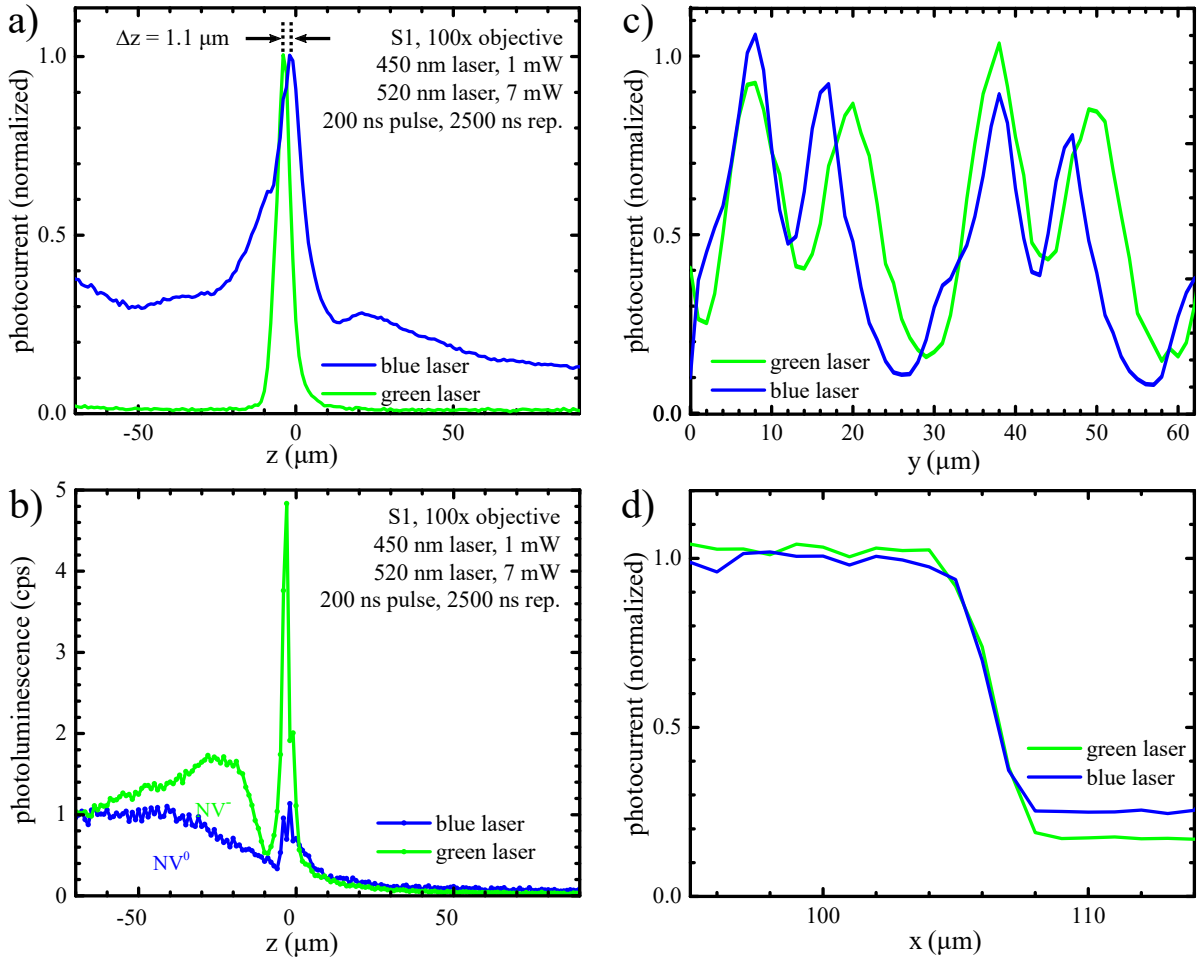


Figure 6.1: a),b) Maximal photocurrent and PL signal is observed when the laser spot is close to the surface, allowing for identification of an axial offset. c), d) Overlap of laser spots can be followed from lateral scans across interdigital contacts.

From the signal generated by green laser excitation one deduces the position of the diamond surface with the method described in section 5.2. The photocurrent signal for blue laser excitation is not only shifted slightly in axial direction, but differs characteristically in its shape. A maximum is observed at z shifted by $1.1 \mu\text{m}$ with respect to the green laser, suggesting that the focal length is $1.1 \mu\text{m}$ larger for the blue laser spot than for the green one. Deviation from a collimated laser beam leads to a divergent beam with a different focus and can explain this experimental finding. As we will see later on, there is no quadratic power dependence for the blue laser, resulting in a broader current peak, even though the point spread function is comparable. It can be verified from the data that small laser intensity is capable of producing a detectable photocurrent when the laser is defocused by $100 \mu\text{m}$. In that case the laser illuminates an area of about $210 \mu\text{m}$ in diameter. A large weakly illuminated diamond volume close to metal contacts then

generates photocurrent under blue laser illumination whereas a higher green laser power density does not produce detectable photocurrent.

The PL signal exhibits pronounced maximums at the same positions as the photocurrent signal does. The shape differs characteristically, since under 450 nm illumination no longer NV⁻ but NV⁰ is the preferred charge state, due to a more efficient NV⁻ ionization by 450 nm photons [19].

Having defined the surface plane the relative lateral position of both laser spots can be minimized by shifting the blue laser spot in *x*- and *y*-direction. Micrometer drives on kinetic mirror mounts allow for precise manual alignment. Figure 6.1 c) exemplarily depicts the laser-induced photocurrent signals after laser alignment in *y*-direction. Since the axial scan has shown the difference in focal length for the lasers, an objective working distance is chosen where both lasers illuminate a comparably large volume. The slightly defocused laser spots generate a broadened photocurrent signal with characteristic maximums and minimums that can be matched. A difference in peak-to-peak distance and peak levels can be explained by two effects. Firstly, different peak heights indicate a deviation of laser propagation direction and diamond surface, an effect that occurs for both lasers. Secondly the peak spacing is about one third larger for the green laser, indicating different spotsizes or photocurrent generation mechanisms. After positioning, the remaining lateral displacement in *y*-direction is about (2.0 ± 0.5) μm , when the left side of the contacts is chosen as measurement position, and (0.2 ± 0.2) μm in *x*-direction, as deduced from photocurrent data (Fig. 6.1 d)). Considering a laser spot displacement < 2 μm in three dimensions and beam diameters of about 2-3 μm under the given experimental conditions even a partial overlap of both lasers is not guaranteed. For the following experiments we chose a working distance where both laser spots penetrate the sample by at least 1 μm creating a situation with increased partial overlap of illuminated detection volume. Basically the method described here allows for precise determination of laser spot sizes, positions and directions by interpreting three-dimensional photocurrent scans with a resolution close to the diffraction limit.

6.1.2 450 nm Laser Photoionization of the NV⁻ Center

In section 5.2.1 the two photon ionization of the NV⁻ center has been discussed for a 520 nm laser. Here, we investigate the NV⁻ center photoionization under 450 nm laser excitation with the same experimental conditions as used for the 520 nm excitation in section 5.2.1. The blue photon energy $E_{\text{ph}} = 2.76$ eV is now higher than $E_{\text{ph}} = 2.38$ eV of green photons. The experimental finding of a linear photocurrent and PL

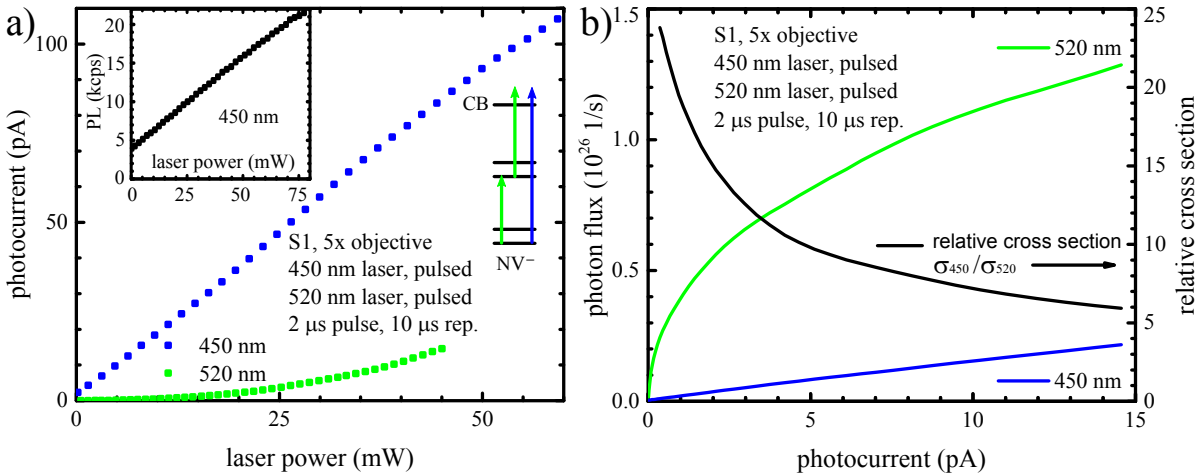


Figure 6.2: a) Blue photons promote electrons directly from NV^- to the conduction band. The observed linear power-dependence suggests a process dominated by one photon excitation, as visualized in the inset. For comparison the previously discussed two photon ionization by a 520 nm laser is shown. b) The cross section inversely proportional to photon flux is larger for 450 nm irradiation and varies with the photocurrent level. The small photocurrent offset arising from the amplifier, is corrected in b).

dependence on laser power is shown in Fig. 6.2 a). The origin of the nonnegligible offset in the PL data can not be assigned to a background signal and is not yet fully understood.

From the detection of photocurrent itself it is concluded that both ionization of NV^- and $\text{NV}^0 \rightarrow \text{NV}^-$ recharging are driven by 450 nm photo-absorption. The photon energy is with 2.76 eV only slightly larger than half of the diamond band gap energy. For the characterization of the dependence of the photocurrent on the laser power homogeneous illumination of diamond is realized with the 5x objective. In order to suppress pulse artifacts a pulse length much longer than the internal transition times is used. A value of $t_{\text{ion}} = 2 \mu\text{s}$ is chosen at a pulse sequence repetition time of 10 μs . A linear power dependence for 450 nm photoionization suggests that one optical transition is rate limiting. Due to a high density of states in the valence band electron excitation is faster than ionization from a defect state within the band gap. This is the same argument as used for the previously discussed 520 nm photoionization in section 5.2.1. Thus the rate limiting transition is identified to be $|1\rangle, |2\rangle \rightarrow \text{CB}$ for 450 nm photons. However, we cannot experimentally exclude a photocurrent contribution from nitrogen donor ionization. The argument allowing for a neglect of N_s^0 photocurrent cannot be the ionization rate but a small $\text{N}_s^+ \rightarrow \text{N}_s^0$ recombination rate of conduction band electrons. A two photon absorption process for valence band electrons over virtual states

in the band gap can also be neglected. This argumentation can be concluded with the experimental finding of a $\text{N}_s^+ \rightarrow \text{N}_s^0$ recombination rate in the range of Hertz, several orders of magnitude smaller than the presumed N_s^0 ionization rate [33]. Another finding is that the detected photocurrent excited by 450 nm photons is larger by more than one order of magnitude for $P_{\text{ion}} < 40$ mW compared to 520 nm excitation (Fig. 5.3 a)). With quadratically increasing photocurrent for the green laser this ratio decreases. The photo-absorption cross section has been investigated for type IIa and CVD diamond as a function of E_{ph} by Rohrer [28]. A constant photocurrent method (CPM) was utilized, where the photocurrent is stabilized at a constant level as E_{ph} varies. In the CPM the Fermi level and thus carrier lifetimes are constant, which results in an inverse dependence of the photoabsorption cross section on the photon flux [34]. The photon density required to keep a certain photocurrent is measured and shown to be a relative measure of cross section of the photoionization as a function of E_{ph} . The cross section is reported to rise significantly by a factor of 2-4 when increasing E_{ph} from 2.38 eV to 2.76 eV [35], [36]. The samples used there had nitrogen concentrations between 6 and 35 ppm. Several broad absorption bands were observed, one of them corresponding to nitrogen impurities at 2.3 eV, and could not be described by a theory including single unbroadened impurity levels [36]. We can reconstruct data similar to a CPM measurement by plotting the data of Fig. 6.2 a) as a function of photocurrent and converting the laser power to a photon flux (Fig. 5.3 b)). From the photonflux inverse to the cross section a relative cross section for 450 nm and 520 nm excitation can be obtained. When the CPM results are compared it has to be noted that [N] in our sample is about an order of magnitude lower than [N] in the samples used by Rohrer. The reported relative cross section is in agreement with our findings assuming a quadratic power dependence for 520 nm laser-induced photocurrent when P_{ion} is set to 80 mW at a photocurrent level of 60 pA.

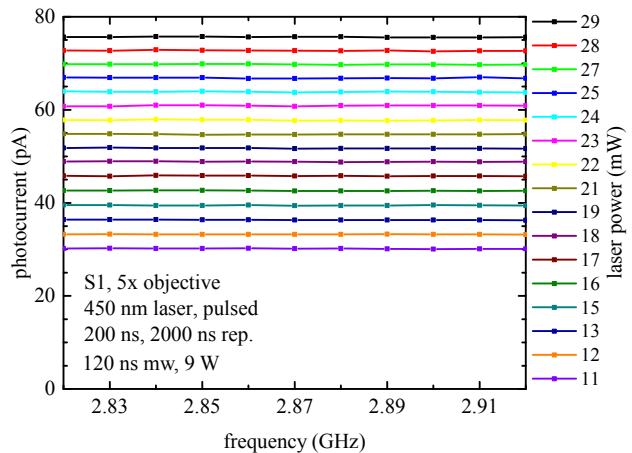
6.1.3 Pulse Sequence for Green and Blue Laser Assisted pEDMR on NV⁻ Centers

A similar experiment according to the previously discussed pEDMR under 520 nm laser excitation is set up with the 450 nm laser. The pulse sequence used is basically the same as in section 5.3.2. Photoionization pulse parameters P_{ion} and t_{ion} are close to those settings for maximal pEDMR contrast of about -13 % under green illumination.

For a range of blue laser powers $P_{\text{ion}} = 11 - 29$ mW both pEDMR and ODMR is recorded (Fig. 6.3). For none of the data sets a significant spin contrast ≥ 1 % is detectable. We

Figure 6.3:

No pEDMR contrast can be detected when blue laser induces NV⁻ ground state photoionization and recharging, NV⁰ → NV⁻.



note that a 450 nm laser-induced PL signal is detected, as already mentioned in section 6.1.2. Observation of no ODMR contrast can be interpreted as follows: If electrons are excited to states $|3\rangle$ and $|4\rangle$, they would undergo spin dependent inter-system crossing (ISC) into $|5\rangle$, from where they relax dominantly nonradiatively. This transition reduces the observed PL intensity. Since no spin contrast is observed, one concludes that the observed PL signal does not originate from the NV⁻ PL spectrum but the NV⁰ PL spectrum. In fact it is known that $\text{NV}^0 \rightleftharpoons \text{NV}^-$ charge state conversion depends on the excitation wavelength [19], [37]. For photoexcitation at 450 nm the dominant charge state is NV⁰ [19]. Further, no NV⁻ ODMR for blue laser excitation has been reported in the literature. However, a more detailed analysis of the PL signal can only be done with further, spectrally resolved, PL data. When the 450 nm laser-induced photocurrent is considered, similar arguments as for the PL discussion can be used. The main part of photocurrent can be attributed to NV⁻ → NV⁰ conversion and the absence of spin selectivity can be attributed to photoionization from the NV⁻ ground state, independent of the spin.

In a next step a pulse sequence is introduced where both processes, NV⁰ → NV⁻ conversion and NV⁻ → NV⁰ ionization, are combined by integrating two lasers in the experiment. The readout pulse sequence is designed to consist of a 520 nm laser shelving pulse followed by a 450 nm ionization laser pulse and is concluded by a set of NV⁰ recharging pulses, as depicted in Fig. 6.4 (top). Using results from the pEDMR optimization (see section 5.3.2) and from a report on efficient spin-to-charge conversion as an estimate for starting conditions, values of 50 ns for shelving pulse duration, 20 ns for the ionization pulse and 12 ns for the delay are chosen at intermediate laser powers [38]. To adapt the laser intensities the total photocurrent integrated over many pulse sequences repetitions is investigated in Fig. 6.4 a). At zero blue laser power (P_{blue}) the quadratic phococurrent dependence on green laser power (P_{green}) can be identified on the left vertical axis, as

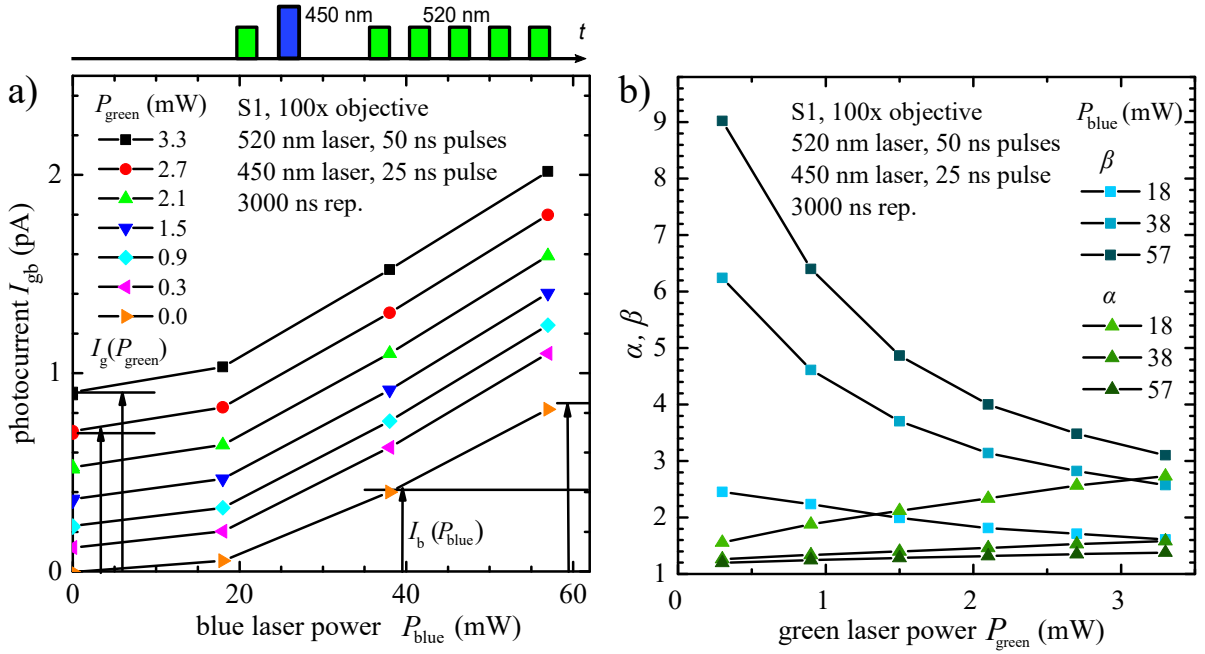


Figure 6.4: a) A pulsed sequence designed for pEDMR experiments is tested for different laser powers. b) Interactions of both lasers at the NV⁻ center occur as non-linearity of the coefficients introduced here.

discussed in section 5.2.1. Accordingly a superlinear photocurrent dependence for the blue laser is represented by the lowest data set along the horizontal axis, in contrast to the observed linear dependence shown in section 6.1.2. Deviations from linearity stems from inaccurate determination of the laser power, which depends strongly on intensity, duration and repetition rate and has not been calibrated separately, but extrapolated from a related calibration measurement. Especially for very short laser pulses of pulse length < 50 ns more reliable data obtained by investigation of the pulse shape and pulse intensity is required for sophisticated research.

At the first sight the photocurrent signal seems to be a superposition of the photocurrent induced by single lasers. That would exclude any interaction of green and blue laser light within a pulse sequence. A simple model with two characteristic parameters is introduced allowing for more detailed investigation of the interaction. The total observed signal I_{gb} is compared to the photocurrent contribution I_g and I_b attributed to the green and blue laser separately, respectively. Parameters α and β are defined as¹

$$\alpha = \frac{I_{gb} - I_g}{I_b} \text{ and } \beta = \frac{I_{gb} - I_b - 5/6 \cdot I_g}{I_g/6}, \quad (6.1)$$

¹The fractions 5/6 and 1/6 are adapted to the pulse sequence consisting of 6 pulses that are assumed to contribute equally and independently to I_g .

and describe a normalization of the photocurrent induced by the very first pulse for each laser in the pulse sequence. Without any interaction, that is $I_{gb} = I_g + I_b$, both parameters α and β are equal to one. Any deviation from one has to be attributed to nonlinear effects and increases the parameter. Figure 6.4 b) shows α and β as a function of P_{green} for different P_{blue} . A parameter of our model with dependence on both laser powers indicates occurrence of non-linearities.

Before discussing physics the errors of this evaluation have to be considered. Normalization on small currents gives rise to big multiplicative errors. Further the attributed laser powers are prone to error and the effective overlap of laser spots remains unknown, allowing only for limited quantitative analysis. For α a value slightly larger one is found, increasing weaker than linearly with P_{green} . The increase is less pronounced for high P_{blue} , suggesting that at high P_{blue} the blue laser dominates all ionization and recharging processes. For β the photocurrent contribution with respect to the green laser is enhanced by a factor of up to 9 for high blue laser powers $P_{\text{blue}} = 57$ mW, whereas the green laser power is low ($P_{\text{green}} < 0.5$ mW). This corresponds to a picture where the green laser effectively induces $\text{NV}^0 \rightarrow \text{NV}^-$ recharging but not ionization, that is dominated by the blue laser. We can compare this experimental finding to a recent report on spin-to-charge conversion utilizing two lasers, a 532 nm cw laser and a pulsed 450 nm laser, proclaiming independent control of pEDMR signal and pEDMR contrast up to -9 % [39]. The authors argue that both ionization and recharging are induced by the pulsed blue laser, whereas the green laser only shelves electrons into the dark state. For $P_{\text{green}} \rightarrow 0$ the limit of the pEDMR contrast under blue laser illumination is zero, which is in agreement with our observation (Fig. 6.3).

A more complex experiment is conducted to identify the nature of the NV⁻ ionization processes in terms of spin sensitivity. To the previously presented pulse sequence just a microwave pulse is added to initialize the NV⁻ center spins. Simultaneously recorded pEDMR and ODMR can be analyzed and allow to identify three different physical regimes for the spin contrast. Figure 6.5 a) depicts pEDMR data for small P_{green} . For even lower P_{green} no pEDMR contrast is detectable. According to the concepts presented in section 5.3 the contrast increases with P_{green} , but is lowered by the additional influence of the last five recharge pulses in this extended pulse sequence.

A significant contrast reduction occurs for large blue ionization powers above 20 mW. At this threshold 450 nm photoionization begins to outperform photoionization driven by the 520 nm laser. The most probable charge state becomes NV⁰ and any NV⁻ population is immediately converted into NV⁰ again. In the limit of very high P_{blue} where P_{green} is negligible the contrast will disappear, as already discussed in the case of

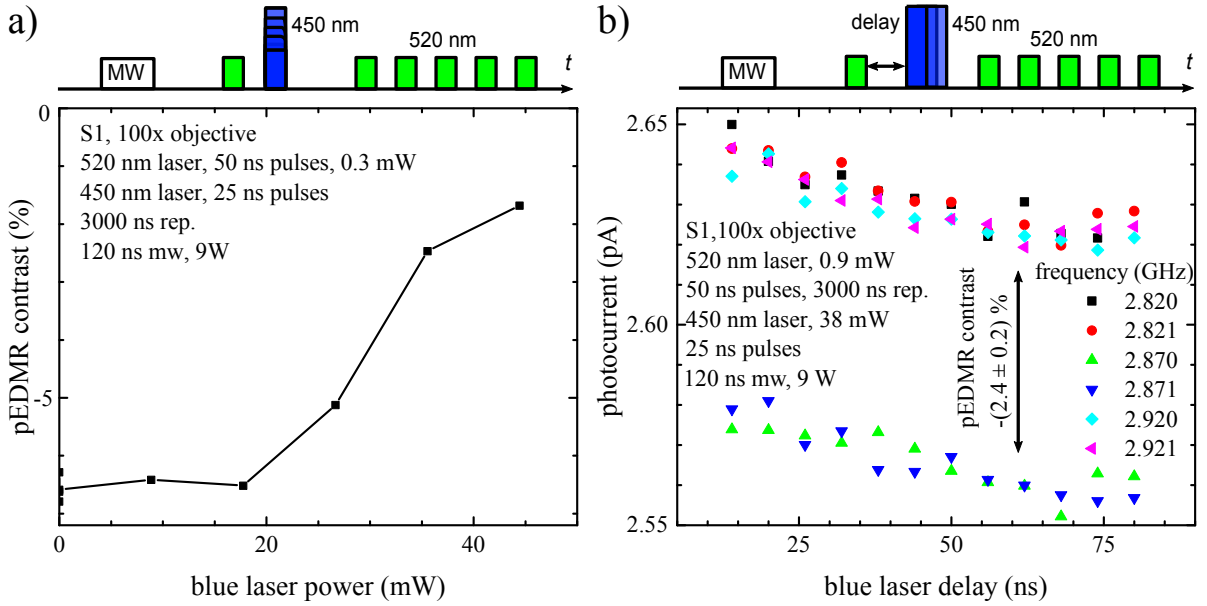


Figure 6.5: a) Combined laser illumination shows quenching of pEDMR contrast under strong blue laser excitation. There, regardless of the spin state NV⁻ ground state electrons are excited to the conduction band. b) Variation of the 450 nm laser pulse delay shows no characteristic dependence on the laser power, supporting the model of an independent ionization process of the NV⁻ center. Resonant data is depicted in green and dark blue.

purely blue laser-induced pEDMR. The effect of spin contrast reduction is also observed in the pEDMR data and can be identified to begin at the same threshold as for ODMR and at which 450 nm photoionization sets in (Fig. 6.4 a)). For PL the underlying mechanism for a signal reduction and thus spin contrast reduction is a decreasing fraction of nitrogen vacancy centers in the NV⁻ charge state with respect to NV⁰, from which PL differs in intensity and is not detected with the same efficiency. Since this experiment was conducted with the uncertainty of laser spot overlap and resulting photocurrent generation in independent volumes leads to a pEDMR contrast reduction a repetition of the very same experiment after precise laser alignment is of interest.

A test experiment underlining insufficient overlap of the volumes of photocurrent generation was conducted by analysing the effect of the time delay between the first two laser pulses of the pEDMR pulse sequence discussed in this section (Fig. 6.5 b)). Resonant and off-resonant pEDMR data is plotted as a function of the pulse delay time. A small decrease of the signal amplitude is observed for all data traces, whereas the pEDMR contrast is constant within the measurement uncertainty. Since the photocurrent signal change with respect to time delay is below 1 % it can be assumed that the photocurrent

generated by the blue laser is mostly independent of the previous green laser-induced photoionization, in agreement with a weak partial overlap. However, the small time dependence observed can be attributed to relaxation processes of the NV⁻ center excited by the 520 nm laser. Theoretically the partial lifetimes 15.8 ns and 15.9 ns of states |3⟩ and |4⟩, respectively, would be expected. This can not be verified by the experimental data since exponential fits did not converge.

6.2 Discussion of a Dual Laser Photoionization Protocol prohibiting N_s⁰ Ionization

In section 5.3.2 the effect limiting pEDMR contrast to a value close to -20 % is assigned to be N_s⁰ ionization. In the following, the absence of a N_s⁰ related photocurrent is presented for optical excitation with a near-infrared (NIR) laser with E_{ph} slightly smaller than the nitrogen donor ionization energy [36]. Our finding is in agreement with other independently reported results and allows to circumvent the limiting effect not by changes of the diamond substrates or NV⁻ center creation process but by adaption of the pEDMR readout method [33].

6.2.1 Laser Alignment

For a homogeneous illumination the 5x objective is chosen. Excitation laser wavelengths are 520 nm for the green laser and 785 nm for the NIR laser. Pure green illumination generates a photocurrent, whereas the NIR laser does not. Therefore alignment was optimized using a material with lower band gap, SiC, where 785 nm photons generate a photocurrent by ionization of the single silicon vacancy in a process comparable to NV⁻ center ionization in diamond [40]. In diamond the 5.45 eV of band gap energy is overcome by in total four photons of 2.34 eV. Accordingly in SiC the band gap of 3.23 eV can be overcome by an ionization and recharging process including 1.58 eV photons [41]. A first photon excites, a second ionizes and subsequently photons recharge the defect into the initial state. Another photocurrent contribution comes from ionization of substitutional nitrogen. Nitrogen in 4H-SiC is a shallow donor with ionization energy of 45 meV which is low compared to previously discussed defect levels in SiC or diamond [42]. Conditions for operation of the silicon carbide MSM detector are adopted from the diamond device.

The same procedure as for the laser spot alignment on diamond can be applied on SiC. This time the 5x objective illuminates a larger area, allowing for a better overlap of volumes illuminated by the green and NIR lasers. When the SiC sample surface is in

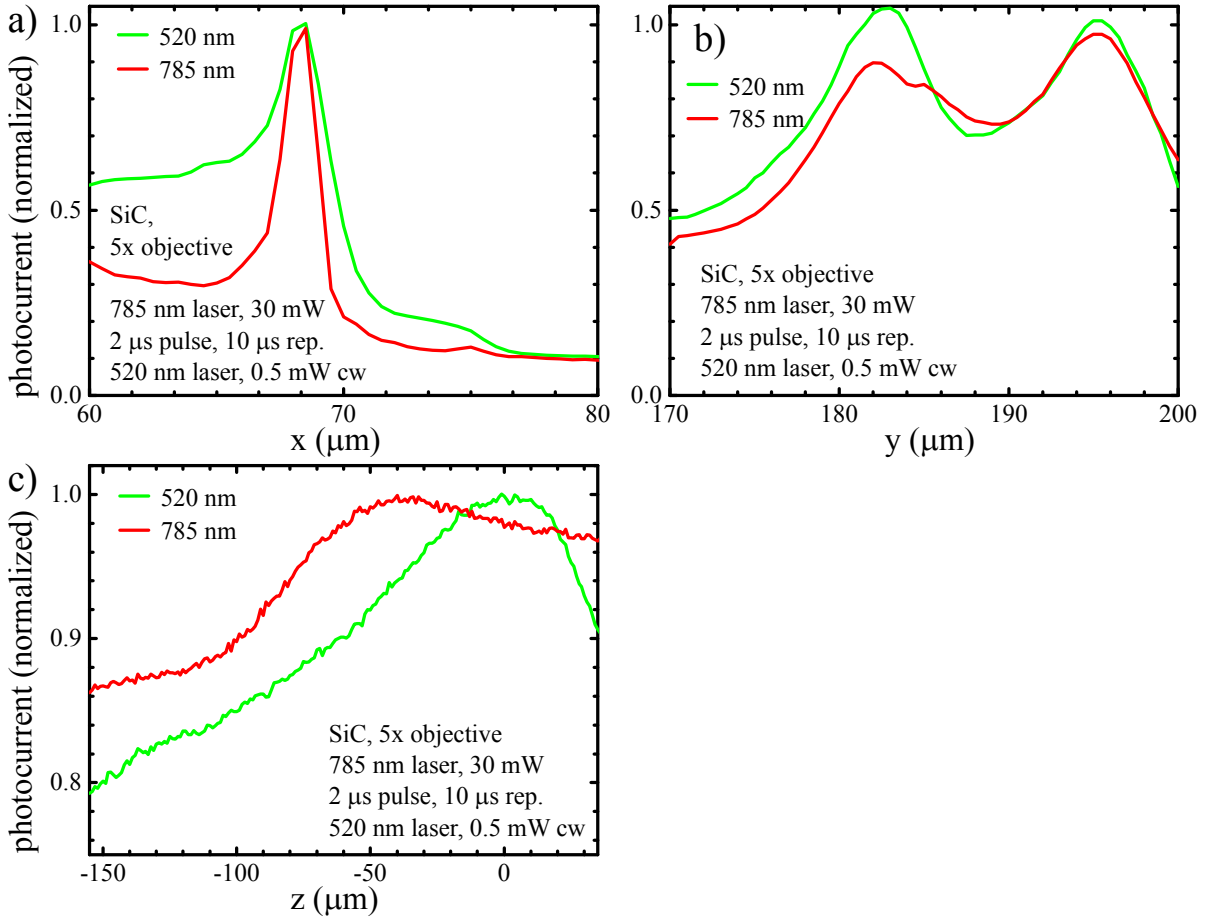


Figure 6.6: Alignment of NIR and green laser. a), b) Scanning across interdigital contacts allows to determine the relative laser position offset. c) The axial spot positions deviate by $(35 \pm 5) \mu\text{m}$.

focus, a lateral x -scan parallel to the interdigital contacts is performed. Data after NIR laser alignment in x -direction is shown in Fig. 6.6 a). The feature at 68 μm marks the inner edge of the positively biased contact. Towards higher z there is a small photocurrent detected up to 75 μm and a drop to an absolute minimum for even higher values. The metal contact prohibits photocurrent generation by covering the detector material underneath. From the still increased photocurrent in the range $z = 69 - 75 \mu\text{m}$ laser spot blurring of up to 6 μm can be deduced. This value is acceptably close to 9 μm , the expected spot size for the 5x objective and a 785 nm laser. In y -direction the alignment procedure is repeated, resulting in a good match when scanning between two negative and one positive interdigital contacts at positions 175, 205 and 190 μm , respectively (Fig. 6.6 b)). Maximal signal is expected close to the positive contact, the width is increased as a consequence of the spot size.

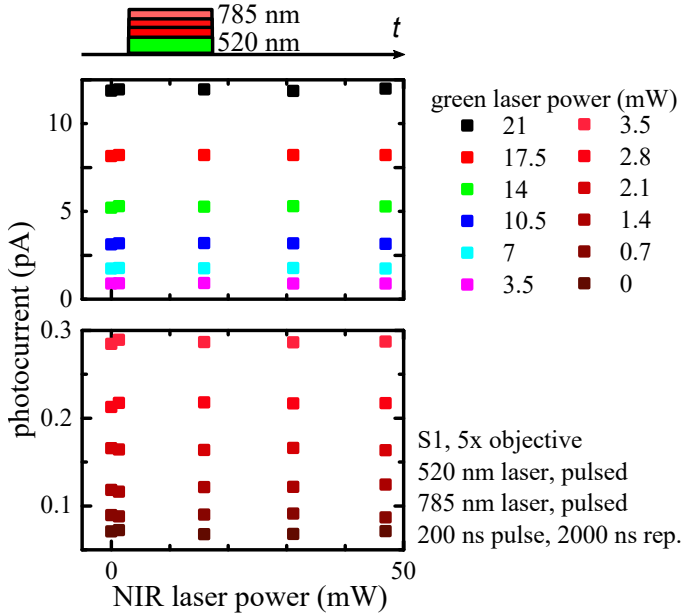


Figure 6.7: No significant change of photocurrent was observed when an NIR laser and a green laser were focused together on the sample. The reason for the independence observed here is insufficient alignment accuracy. However, one finding is that the NIR laser does not induce photoionization, explicitly it does not ionize N_s⁰.

From the match of the peak positions in *x*- and *y*-direction for the green and the NIR laser it can be deduced that in the focal plane the NIR laser spot center deviates by less than 1 μm , which is much smaller than the spot sizes (Fig. 6.6 a), b)). In axial direction a correction of focal depth is not possible in our setup. However the deviation can be measured (Fig. 6.6 c)), revealing that the green laser has a 50 μm higher focus length than the NIR laser. When the *NA* of 0.15 is expressed as an angle a laser spots widening of 4 μm in the focal plain per 25 μm in axial direction can be calculated. For further experiments an intermediate *z*-position of -17 μm was chosen. Estimated spot diameters for this setting are 17 μm for the NIR and 14 μm for the green laser.

6.2.2 Green Near-Infrared Pulse Sequence

In a pulsed experiment the photoionization in diamond by a NIR laser is investigated. The photon energy is smaller than the energy of the N_s⁰ absorbtion band at 2.3 eV [36]. One tries to ionize the optically excited NV⁻ center that is energetically about 0.6 eV below the conduction band, as one can deduce from E_{ph} of ionizing 450 nm photons and the ZPL emission at 637 nm. Further, the optically excited NV⁻ center

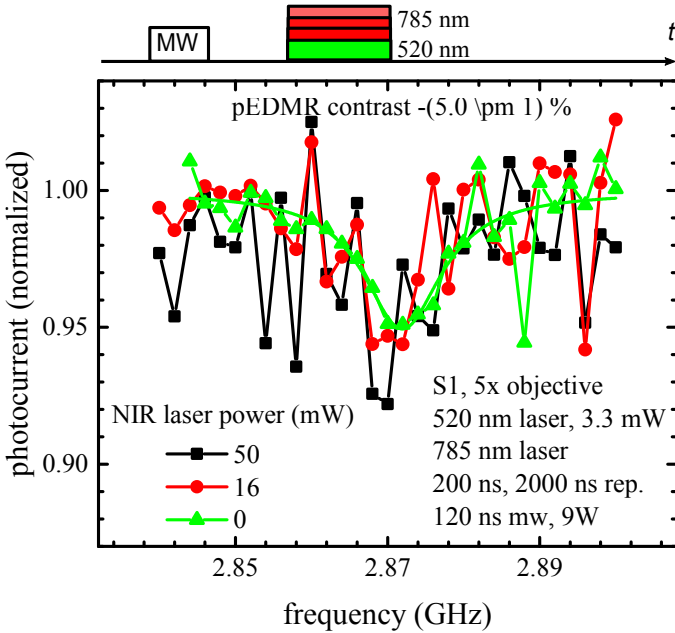


Figure 6.8:

pEDMR contrast under simultaneous green and NIR laser illumination. Additional noise is introduced by the NIR laser, acting as an uncontrolled heat source.

is reported to be 2.7 eV below the band gap, being studied in an indirect method [19]. Another group of scientists deduces from cross section measurements an ionization energy of 2.66 - 2.70 eV [39]. The NV^- center model would allow green photons to recharge and excite the NV^- center. A powerful NIR laser pulse could then be applied to promote the electron to the conduction band. Such a laser pulse will not ionize N_s^0 because it is energetically forbidden, contrary to 520 nm ionization. However, the data in Fig. 6.7 provides no evidence for such a process. Independent of the NIR laser power all detected photocurrent is induced by the green laser. The NIR laser does not ionize any defects at all, especially not N_s^0 , however also not NV^- . In a pEDMR experiment no effect on the pEDMR contrast could be measured as a function of the NIR laser power. Figure 6.8 shows a weak spin contrast of -3 % exclusively linked to illumination with the green laser. This contrast remains unchanged, even under NIR laser illumination, but the noise in the system increases drastically with NIR laser power P_{NIR} . The strong increase in noise argues against Johnson-Nyquist noise as a source, which is only linearly proportional to the temperature (T) [32]. An effect more sensitive to T is thermionic emission of electrons into the contacts. The current through a metal-semiconductor contact is characterized by the Richardson constant and a quadratic T dependence [16]. The quadratic T dependence allows temperature fluctuations to be still considered to influence the photocurrent amplitude more strongly, possibly induced by an unstable NIR laser mounting. A mismatch of the laser spots was recognised that shifted in an uncontrolled manner over days, further supporting this assumption.

Chapter 7

Conclusions and Outlook

On the one hand, the purpose of this master thesis was to build a spectrometer for NV⁻ spin detection with optically and electrically detection. The dynamics of the NV⁻ spin-to-charge conversion was studies and optimized in a previous work conducted at our institute by Hrubesch [12]. With that knowledge a new spectrometer could be tested and reproduce comparable results.

In spin resonance experiments it was demonstrated that electrical readout of the NV⁻ center in diamond provides a spin contrast that can compete with optical readout (section 5.3.1). The linewidth of the spin resonance experiments is slightly different in our experiments, an effect that can be attributed to differences in detection volume and excitation intensity, as they occur only specifically in our experiment. The amplitude of spin contrast was maximized to -13.5 % in a type IIa diamond sample in this thesis. This relates to conditions where the 520 nm laser effectively pumps electrons into the shelving state where they are protected from ionization for a time longer than the laser excitation pulse.

On the other hand ionization of the NV⁻ center was investigated in order to further increase the contrast of spin-to-charge conversion by adapting photon energies to energies related to the NV⁻ energy levels. From photocurrent spectroscopy experiments (section 6.1.2) it can be deduced that one photon ionization of the NV⁻ center in its ground state is achieved by a 450 nm laser. Extended experiments with a NV⁻ readout scheme utilizing a 520 nm and 450 nm lasers could not improve the spin contrast. As the ionization power of the blue laser becomes significant, spin contrast is reduced, in accordance with an ionization mechanism completely independent of previous NV⁻ center initialization. Also ionization from the shelving state by a 450 nm laser cannot be excluded by analysis of our data. It can be concluded, that at an intermediate shelving power of less than 0.5 mW of green laser no contrast improvements were observable. The dynamics of a two laser pulse sequence consisting of a 520 nm shelving pulse followed by a 450 nm photoionization pulse and serveral 520 nm recharging pulses may

be studied in more detail to identify the preferred NV^- charge state during the pulse sequence. Of major importance for such experiments is the laser power and pulse shape when experimental data has to be fitted to new models. To sum up, our findings are in agreement with a strong ionization behavior of a 450 nm laser resulting in a dominant NV^0 configuration whereas 520 nm laser converts NV^0 into NV^- and drives the shelving process.

Optical experiments show that utilization of a multi-photon-excitation mechanism can improve spin contrast and provide a high signal-to-noise ratio for room temperature single-shot spin readout [38], [43]. In analogy to optical detection techniques one could improve the electrical readout scheme using a multi photon spin-to-charge conversion assisted by a red or NIR laser. Careful analysis of the laser powers allows for identification of nonlinear effects and saturation regimes. Ultimately a combination with single electron transistors fabricated on top of single NV^- centers opens a route to electrical demonstration of single shot spin-to-charge conversion at room temperature.

Finally I sum up possible extensions and improvements for the setup presented in this work (chapter 4). The optical detection allows to measure NV^0 and NV^- photoluminescence, albeit without the possibility to distinguish the charge state spectroscopically. Additional usage of appropriate PL filters (e.g. bandpass filters) would allow for better distinction between different PL emitting defects. Filters could be mounted on a rotatable wheel in the optical path before the APD. Another alternative would be recording the time dependence of the PL signal. So far time dependence is only discussed as a result of the pulse sequence. The benefit would be a time-resolved PL signal that reveals lifetimes of the PL emitters. This opens an alternative approach to identify the PL emitter without the need of recording a spectrum, given that the half times are known. The time resolution can be obtained from the APD performance and the readout device. Currently, the relevant hardware specifications are 10 ns APD pulse width, a detector dead time of 22 ns and a 80 MHz readout card. Theoretically these parameters result in a 12 ns time resolution when integrating PL over many pulse sequences.

So far laser reflections from the sample surface are partially detected by the APD. Better filters are required to suppress the excitation source efficiently and to transmit only PL photons. For the alignment of the laser spots with respect to the sample structure and eventually a second laser optical feedback were helpful, as is accelerates the laser alignment process. By mapping the sample surface on a CCD-camera chip one could easily obtain such an optical feedback. The concept is to insert an additional beam splitter in the optical path of the lasers, for example using a 90/10 beam splitter. An neutral density filter protects the camera chip that detects the image of the sample

surface. To obtain a resolution better than the minimal laser spot size an appropriate microscope objective and CCD-chip pixel size have to be chosen. Another advantage of a camera imaging system is a simplified sample positioning. Once there is a beam splitter in the optical excitation path, it can be used to couple in a light source and to use surface reflections to bring the sample into focus at the desired structure, benefiting from fast optical feedback in video quality. One could imagine an aligning procedure, where firstly one uses the light source to position the sample on the optical table. When the sample image is sharp, it is in the objective's focus. When two lasers are to be aligned a neutral density filter can be inserted in the camera path. Using a pulse sequence where alternating lasers illuminate the sample at a slow rate that is not too fast for the human eye the laser positions can be readjusted.

Laser pulse shape and amplitude are not well defined for short pulses with $t_{ion} < 50$ ns. The power calibration conducted so far is not recommended for further experimental studies aiming for a precise description on laser power due to the high errors that arise only by small changes in the pulse sequence. For example, implementing an additional green laser recharge pulse results in a chance of the repetition rate or varies the waiting time before repeating the pulse sequence. Anyway, the duty cycle varies and causes deviation from previously conducted calibration. A photodetector in the optical path detecting laser light can track the laser intensity during the measurement and provide information on the actual absolute laser power, when losses in the optics are corrected. Light can be coupled out by using a beam splitter and a powermeter, for example integrated in the optical path before the CCD-camera.

Another, rather minor, disadvantage of the laser driver module is a minimal threshold current that is provided at any time and which causes spontaneous laser diode emission. To circumvent this side-effect currently a small resistor is soldered in parallel to the diode. Below lasing threshold the laser module driver current bypasses the diode through the resistance, while it has no further effect, when the diode is lasing. Another solution without the need of hardware modification is setting the pulse low voltage of the signal generator to a negative value that prevents lasing and does not harm the laser driver circuitry.

When focused laser excitation is discussed both laser spot size and power are important. The shape of the laser spot after the microscope is defined by the incident laser beam profile. Similar spot shapes are especially important, when two laser spots are to be overlapped. Smallest spot sizes are obtained for Gaussian beam profiles, that can be gathered from imperfect light sources by filtering out all non Gaussian contributions. Such a filtering mechanism is provided by a spatial filter consisting of two coplanar lenses and a pinhole in its focus. The optimization of the spot profile is achieved at the cost

of laser intensity, which is reduced by the laser beam components filtered out. Another beam profile adaptation ansatz which basically conserves laser intensity but does not necessarily guarantee a Gaussian beam profile is to utilize an anamorphic prism pair to reduce the elliptic aspect ratio.

Appendix A

Laser Characteristics

A.1 Mathematical Discussion on Laser Calibration

Rectangular pulses from the signal source exhibit finite pulse slopes. The used wave form generator can reduce these triangular flanks to edge times of at least 5 ns. Since most experiments deal with the value of laser power its average dependent on the experimental parameters shall be considered here in detail. An exemplary pulse is depicted in Fig. A.1. The averaged laser power \bar{P} is defined as

$$\bar{P} = \frac{\int_0^T P(t)dt}{\int_0^T dt}, \quad (\text{A.1})$$

where T denotes the integration time, in our case set to the laser repetition time. For simplicity we consider here a linear dependence of the laser driver input voltage on the laser diode current, which is proportional to the optical output power. Figure A.1 a) shows a rectangular laser driver voltage pulse of width w and finite edge time e which can be written as

$$P(t) = \begin{cases} P_0 \cdot \frac{t}{e}, & 0 < t \leq e \\ P_0, & e < t \leq w \\ P_0 \cdot \left(1 - \frac{t-w}{e-t_0}\right), & w < t < w+e. \end{cases} \quad (\text{A.2})$$

Averaging $P(t)$ over time yields

$$\bar{P} = \frac{1}{T} \left[2 \int_0^e P(t)dt + \int_e^w P(t)dt \right] = P_0 \frac{1}{T} \left[2 \frac{e^2}{2e} + (w-e) \right] = P_0 \frac{w}{T}. \quad (\text{A.3})$$

This result can be easily verified by considering the area under the graph of $P(t)$. Typically lasing occurs only above a lasing threshold current corresponding to U_{th} . Primed variables U' and P' are introduced as $U' = U - U_{\text{th}}$ and $P' = P(U') \propto U'$, depicted also in the right hand side of Fig. A.1 b).

Since lasing does not start before U' exceeds 0 the effective interval of lasing is shortened. Mathematically the power can be parametrized as

$$\bar{P}' = \alpha \begin{cases} P_0 \cdot \frac{t}{e - t_0} & , t_0 < t \leq e \\ P_0 & , e < t \leq w \\ P_0 \left(1 - \frac{t - w}{e - t_0} \right) & , w < t < w + e - t_0. \end{cases} \quad (\text{A.4})$$

When evaluating \bar{P}' similarly to \bar{P} one obtains

$$\bar{P}' = \frac{1}{T} \left[2 \int_{t_0}^e P'(t) dt + \int_e^w P'(t) dt \right] \quad (\text{A.5})$$

$$= \frac{P_0}{T} \left[2 \frac{(e - t_0)^2}{2(e - t_0)^2} + (w - e) \right] \quad (\text{A.6})$$

$$= \frac{P_0}{T} \left(w - \frac{U_{\text{th}}}{U_0} e \right) \quad (\text{A.7})$$

$$= P_0 \frac{w}{T} \left(1 - \frac{U_{\text{th}}}{U_0} \frac{e}{w} \right). \quad (\text{A.8})$$

The result may be checked in the mathematical limits

$$\lim_{U_{\text{th}} \rightarrow 0} \bar{P}'(U') = \frac{P_0}{T} w \quad \text{and} \quad \lim_{U_{\text{th}} \rightarrow U_0} \bar{P}'(U') = \frac{P_0}{T} (w - e). \quad (\text{A.9})$$

As one would expect we obtain for $U_{\text{th}} \rightarrow 0$ the initial (A.3) where no U_{th} was taken into account. The other limit can be understood graphically. For very high U_{th} lasing occurs only when U' is maximal for the interval of $w - e$. Concrete values of the lasing threshold are (100 - 200) mV for operation voltages between (100 - 700) mW corresponding to $0.14 \lesssim U_{\text{th}}/U_0 \lesssim 1$. These values lead to the conclusion that the averaged laser power scales as $P_0 w / T$ as long as the laser driver voltage is not too close to the lasing threshold and pulse width exceeds the edge time by far. Otherwise (A.8) may be applied.

A.2 Laser Power Calibration

In this section laser voltage and laser driver voltage shall be used as synonyms for simplicity, even though this nomenclature is nonphysical. Laser intensity is measured either with a Si photodiode (*Thorlabs*, S130C) or a thermal sensor (*Thorlabs*, S401C). For analysis of the pulse shapes a fast Si diode (*Hamatsu*, H9055) with a risetime <1 ns was used. All sensors detect a signal linear in the input power (Fig. A.2). Absolute values obtained from data recorded with the fast Si diode do not represent the absolute laser power, most probably because the laser could not be focused efficiently on the small detector chip. There is an increase in laser driver module performance observed at very high repetition rates, shown in Fig. A.3. Further graphs provide the calibration curves for the individual laser diodes in different operation modes, Fig. A.4 for the 450 nm laser, Fig. A.5 for the 520 nm laser and Fig. A.6 for the 785 nm laser.

A.3 Laser Suppression in the Photon Detection System

A calibration of the APD detection system was conducted. For this purpose a mirror instead of the sample was mounted and the microscope objective was brought into focus. In this configuration a z -scan was recorded revealing the position of the mirror surface. For increasing laser power the light reflected at the mirror that enters the APD system is detected. In Fig. A.7 a) the z -scan exhibits a maximum when the mirror surface is in focus. Interestingly the maximum has a two peak structure, both are equally high and separated by $2.2\ \mu\text{m}$ as can be read from the high resolution measurement in the inset. A z -misalignment by half of this value between the foci of laser excitation and light detection can explain this feature. It can be corrected by readjusting the axial positions in the collection lens system before the APD. Figures A.7 b) and c) show the laser background calibration measurement for two configurations, the first without and the second with the 645 nm long pass filter. The effect of the additional filter is further suppression factor of 3. For better comparison three data sets are shown in each calibration graph for the three characteristic positions of local maximum and local minimum close to the mirror surface.

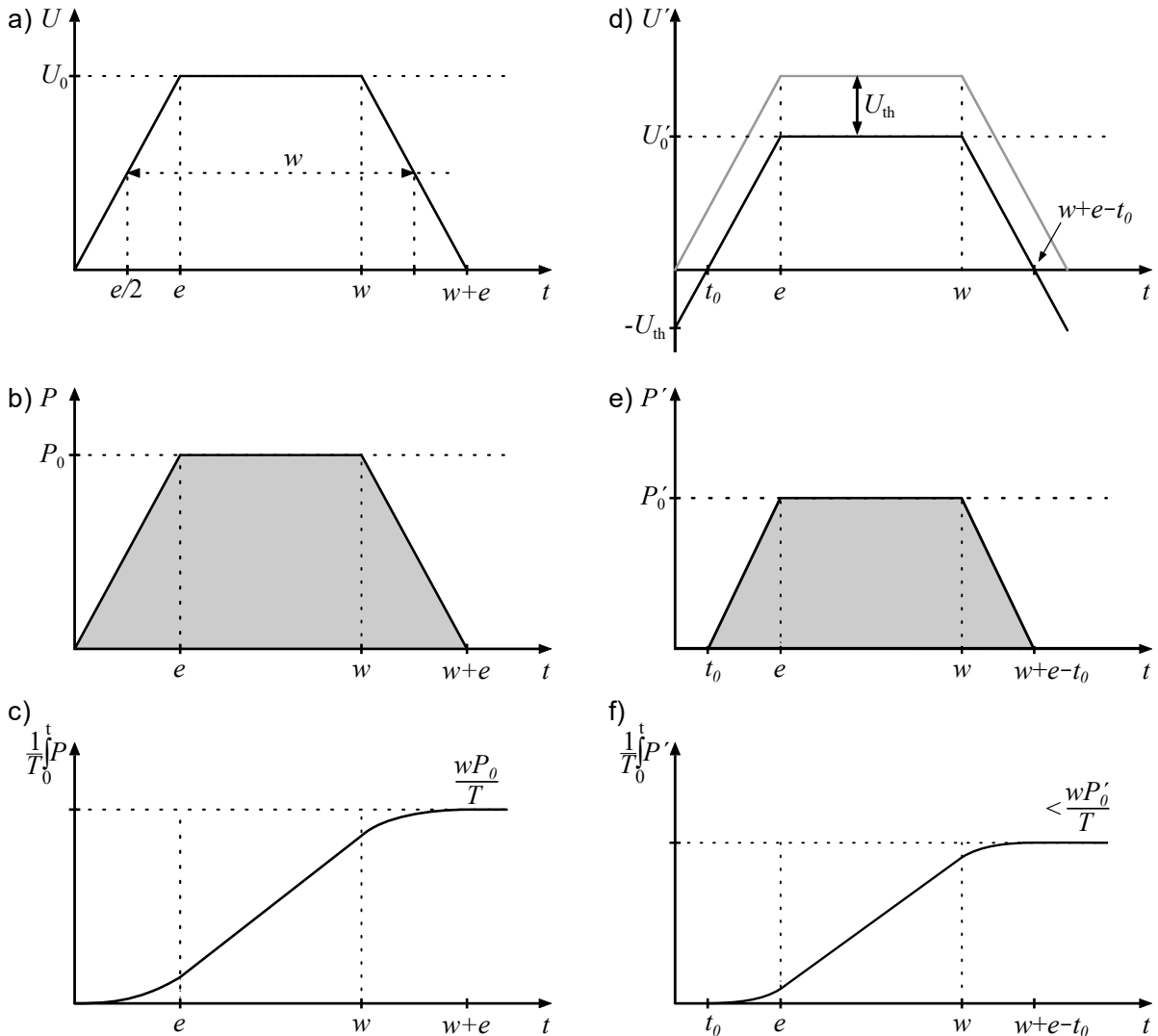


Figure A.1: Averaged laser power for a rectangular pulse with finite pulse slopes. a) Signal as is drives the laser diode and b) assumption for laser output power and c) averaged value. d), e) Since lasing occurs only above U_{th} the effective interval of lasing is shortened. The effect can be better described by introducing U' and P' with proportional relation between them. f) The average laser power is lowered by a factor depending on the edge time and lasing threshold.

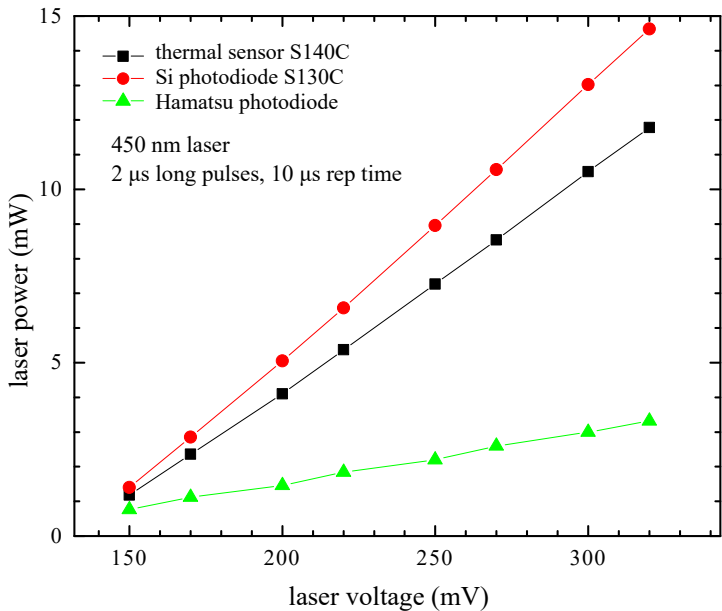


Figure A.2: Sensors used for determination of laser powers in the setup. The fast Hamatsu Si diode was mainly used for pulse shape analysis rather than absolute measurements.

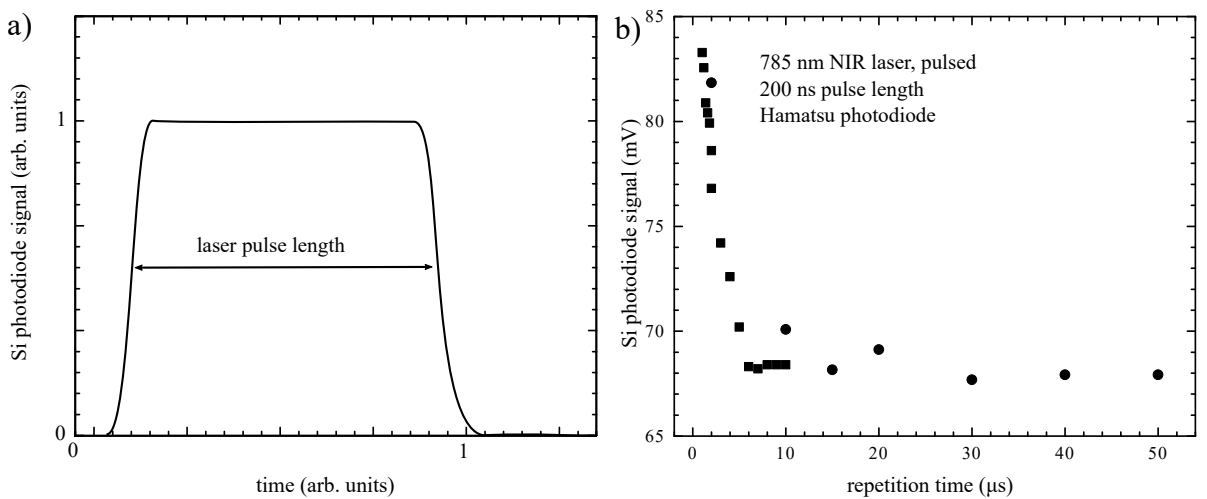


Figure A.3: a) Schematic illustration of the laser pulse shape for a single pulse. b) Experimental data of pulse intensities for the NIR laser. For low repetition times at fixed pulse duration, i.e. high duty cycles, a non-linear increase in lasing power is observed. This effect is attributed to the laser driver.

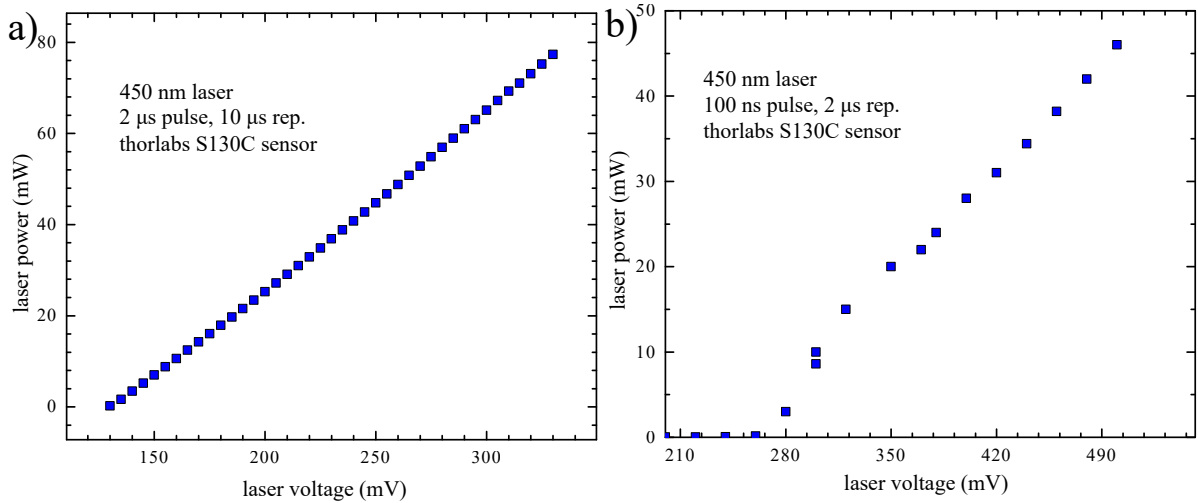


Figure A.4: a) Power calibration for the 450 nm laser for long pulse operation at 2 μ s pulse length and 100 ns pulse length. Intensity is measured with the S130C sensor. The laser power settled at an equilibrium value after several seconds after switch on, when the laser diode temperature saturated. Here, no cooling fan is used.

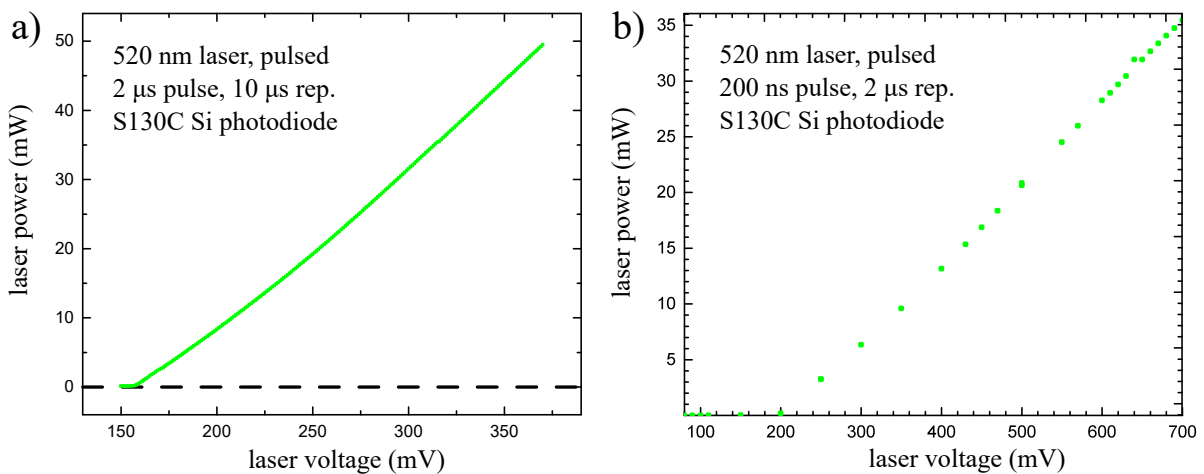


Figure A.5: Characteristics of the 520 nm laser. a) Performance in long pulse mode operation and b) under standard experimental conditions.

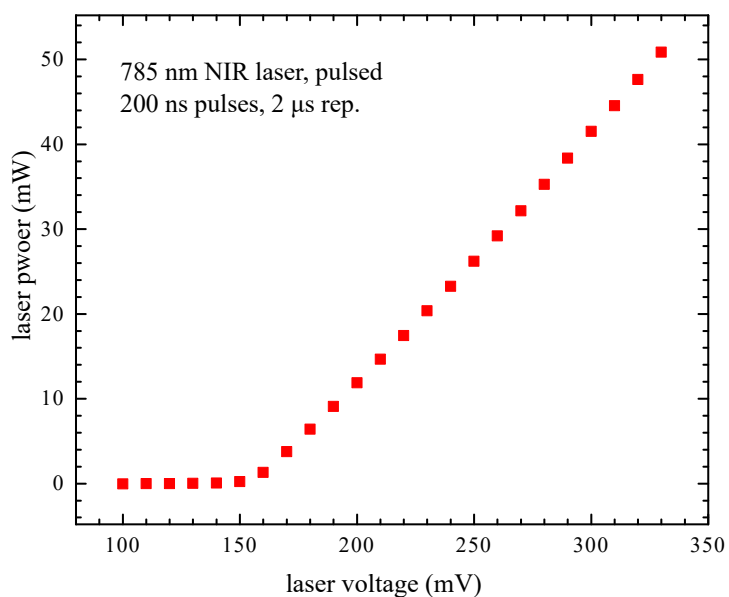


Figure A.6: Characterization of the NIR laser. In the limit of long laser pulses and low duty cycle the 785 nm has a linear output power above the lasing threshold of 155 mV.

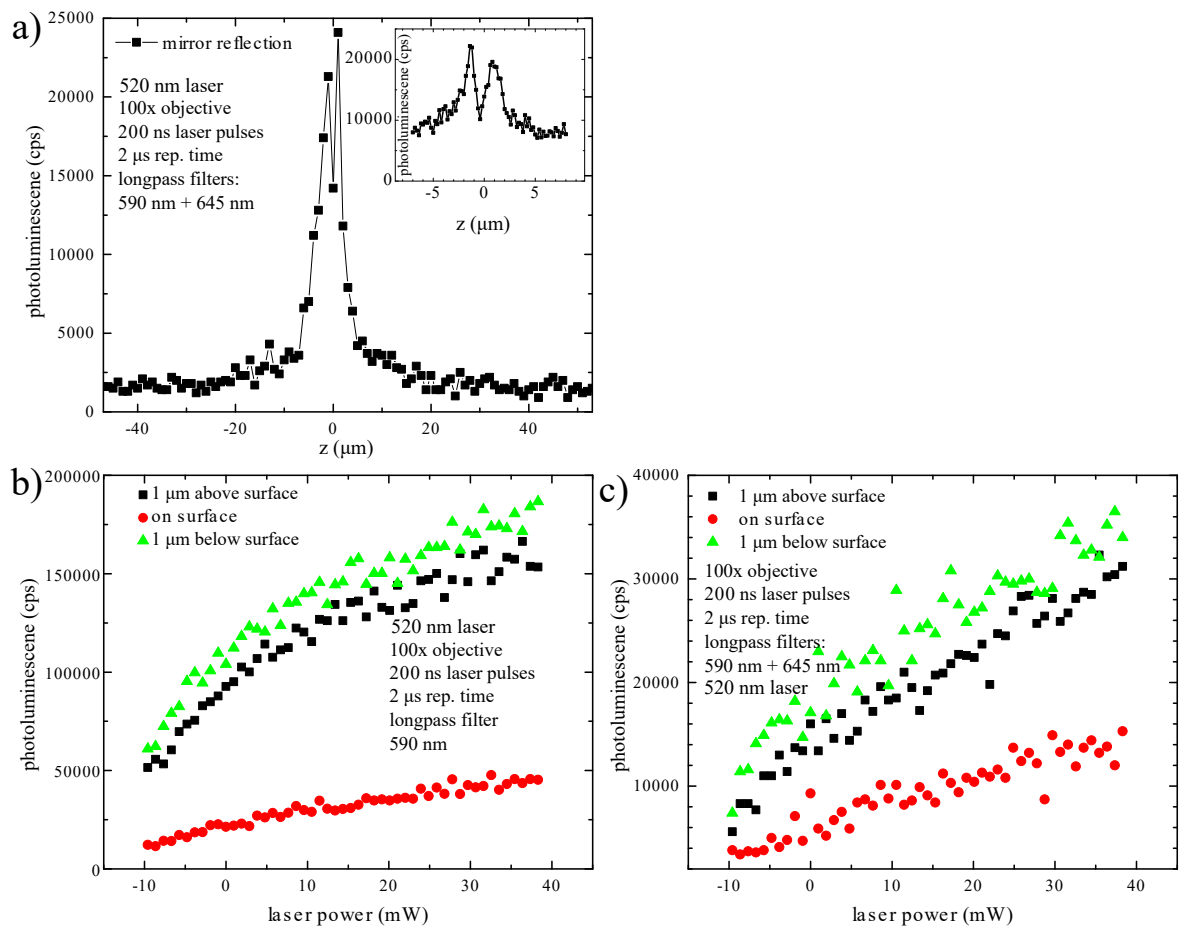


Figure A.7: a) 520 nm laser reflections from a mirror in focus are not suppressed perfectly by the APD filters. b), c) Nominal laser power is plotted versus PL signal for two different long pass filter configurations. Usage of an additional 645 nm long pass filter suppresses the PL count rate by a factor of about five.

Bibliography

- [1] N. Bar-Gill, L. M. Pham, A. Jarmola, D. Budker and h. Walsworth, R. L.: *Solid-state electronic spin coherence time approaching one second*, Nature Communications **4**, 1743 (2013).
- [2] J. T. Muhonen, J. P. Dehollain, A. Laucht, F. E. Hudson, R. Kalra, T. Sekiguchi, K. M. Itoh, D. N. Jamieson, J. C. McCallum, A. S. Dzurak and A. Morello: *Storing quantum information for 30 seconds in a nanoelectronic device*, Nature Nanotechnology **9**, 986 (2014).
- [3] K. M. Itoh and H. Watanabe: *Isotope engineering of silicon and diamond for quantum computing and sensing applications*, MRS Communications **4**, 143 (2014).
- [4] V. M. Acosta, E. Bauch, M. P. Ledbetter, A. Waxman, L.-S. Bouchard and D. Budker: *Temperature Dependence of the Nitrogen-Vacancy Magnetic Resonance in Diamond*, Physical Review Letters **104**, 070801 (2010).
- [5] J. Maze, A. Gali, E. Togan, Y. Chu, A. Trifonov, E. Kaxiras and M. Lukin: *Properties of nitrogen-vacancy centers in diamond: the group theoretic approach*, New Journal of Physics **13**, 025025 (2011).
- [6] P. Maletinsky, S. Hong, M. S. Grinolds, B. Hausmann, M. D. Lukin, R. L. Walsworth, M. Loncar and A. Yacoby: *A robust scanning diamond sensor for nanoscale imaging with single nitrogen-vacancy centres*, Nature Nanotechnology **7**, 320 (2012).
- [7] N. Bar-Gill and A. Retzker: *Observing chemical shifts from nanosamples*, Science **357**, 38 (2017).
- [8] J. Zheng, A. C. Liapis, E. H. Chen, C. T. Black and D. Englund: *Near-unity collection efficiency from quantum emitters in bulk diamond using chirped circular dielectric gratings*, arXiv:1706.07566 (2017).
- [9] J. T. Choy, I. Bulu, B. J. M. Hausmann, E. Janitz, I.-C. Huang and M. Lončar: *Spontaneous emission and collection efficiency enhancement of single emitters in*

- diamond via plasmonic cavities and gratings*, Applied Physics Letters **103**, 161101 (2013).
- [10] A. Brenneis, L. Gaudreau, M. Seifert, H. Karl, M. S. Brandt, H. Hübl, J. A. Garrido, K. H. L. and A. W. Holleitner: *Ultrafast electronic readout of diamond nitrogen-vacancy centres coupled to graphene*, Nature Nanotechnology **10**, 135 (2015).
- [11] E. Bourgeois, A. Jarmola, P. Siyushev, M. Gulka, J. Hruby, F. Jelezko, D. Budker and M. Nesladek: *Photoelectric detection of electron spin resonance of nitrogen-vacancy centres in diamond*, Nature Communications **6**, 8577 (2015).
- [12] F. M. Hrubesch, G. Braunbeck, M. Stutzmann, F. Reinhard and M. S. Brandt: *Efficient Electrical Spin Readout of NV⁻ Centers in Diamond*, Physical Review Letters **118**, 037601 (2017).
- [13] M. V. Hauf, P. Simon, N. Aslam, M. Pfender, P. Neumann, S. Pezzagna, J. Meijer, J. Wrachtrup, M. Stutzmann, F. Reinhard and J. A. Garrido: *Addressing single nitrogen-vacancy centers in diamond with transparent in-plane gate structures*, Nano Letters **14**, 2359 (2014).
- [14] E. A. Ekimov, V. A. Sidorov, E. D. Bauer, N. N. Mel'nik, N. J. Curro, J. D. Thompson and S. M. Stishov: *Superconductivity in diamond*, Nature **428**, 542 (2004).
- [15] J. Isberg, J. Hammersberg, E. Johansson, T. Wikström, D. J. Twitchen, A. J. Whitehead, S. E. Coe and G. A. Scarsbrook: *High carrier mobility in single-crystal plasma-deposited diamond*, Science **297**, 1670 (2002).
- [16] S. M. Sze and K. N. Kwok: *Semiconductor Devices* (Wiley, 2007).
- [17] J. Walker: *Optical Absorption and Luminescence in Diamond*, Reports on Progress in Physics **42**, 1605 (1979).
- [18] L. Robledo, H. Bernien, T. van der Sar and R. Hanson: *Spin dynamics in the optical cycle of single nitrogen-vacancy centres in diamond*, New Journal of Physics **13**, 025013 (2011).
- [19] N. Aslam, G. Waldherr, P. Neumann, F. Jelezko and J. Wrachtrup: *Photo-induced ionization dynamics of the nitrogen vacancy defect in diamond investigated by single-shot charge state detection*, New Journal of Physics **15**, 013064 (2013).

- [20] A. Gruber, A. Dräbenstedt, C. Tietz, L. Fleury, J. Wrachtrup and C. Von Borczyskowski: *Scanning confocal optical microscopy and magnetic resonance on single defect centers*, Science **276**, 2012 (1997).
- [21] A. Gali: *Time-dependent density functional study on the excitation spectrum of point defects in semiconductors*, Physica Status Solidi (b) **248**, 1337 (2011).
- [22] P. Siyushev, H. Pinto, M. Vörös, A. Gali, F. Jelezko and J. Wrachtrup: *Optically Controlled Switching of the Charge State of a Single Nitrogen-Vacancy Center in Diamond at Cryogenic Temperatures*, Physical Review Letters **110**, 167402 (2013).
- [23] D. J. Christle, A. L. Falk, P. Andrich, P. V. Klimov, J. U. Hassan, N. T. Son, E. Janzén, T. Ohshima and D. D. Awschalom: *Isolated electron spins in silicon carbide with millisecond coherence times*, Nature Materials **14**, 160 (2015).
- [24] M. H. Levitt: *Spin Dynamics* (Wiley, 2001).
- [25] S. Sotoma, Y. Yoshinari, R. Igarashi, A. Yamazaki, S. H. Yoshimura, H. Tochio, M. Shirakawa and Y. Harada: *Effective production of fluorescent nanodiamonds containing negatively-charged nitrogen-vacancy centers by ion irradiation*, Diamond and Related Materials **49**, 33 (2014).
- [26] S. Pezzagna, B. Naydenov, F. Jelezko, J. Wrachtrup and J. Meijer: *Creation efficiency of nitrogen-vacancy centres in diamond*, New Journal of Physics **12**, 065017 (2010).
- [27] H. Kawarada: *Hydrogen-terminated diamond surfaces and interfaces*, Surface Science Reports **26**, 205 (1996).
- [28] E. Rohrer: *Photoleitungs-Spektroskopie an Diamant* (Schriftenreihe des Walter Schottky Instituts, Garching, 1998).
- [29] M. Young: *Optics and Lasers* (Springer, 1993).
- [30] V. M. Acosta, A. Jarmola, E. Bauch and D. Budker: *Optical properties of the nitrogen-vacancy singlet levels in diamond*, Physical Review B **82**, 201202 (2010).
- [31] P. L. Stanwix, L. M. Pham, J. R. Maze, D. Le Sage, T. K. Yeung, P. Cappellaro, P. R. Hemmer, A. Yacoby, M. D. Lukin and R. L. Walsworth: *Coherence of nitrogen-vacancy electronic spin ensembles in diamond*, Physical Review B **82**, 201201 (2010).

Bibliography

- [32] K. Jensen, V. M. Acosta, A. Jarmola and D. Budker: *Light narrowing of magnetic resonances in ensembles of nitrogen-vacancy centers in diamond*, Physical Review B **87**, 014115 (2013).
- [33] J. Chen, S. Lourette, K. Rezai, T. Hoelzer, M. Lake, M. Nesladek, L.-S. Bouchard, P. Hemmer and D. Budker: *Optical quenching and recovery of photoconductivity in single-crystal diamond*, Applied Physics Letters **110**, 011108 (2017).
- [34] M. Vaněček, A. Abraham, O. Štika, J. Stuchlik and J. Kočka: *Gap states density in a-Si: H deduced from subgap optical absorption measurement on Schottky solar cells*, Physica Status Solidi (a) **83**, 617 (1984).
- [35] E. Rohrer, C. F. O. Graeff, R. Janssen, C. E. Nebel, M. Stutzmann, H. Gütter and R. Zachai: *Nitrogen-related dopant and defect states in CVD diamond*, Physical Review B **54**, 7874 (1996).
- [36] E. Rohrer, C. Nebel, M. Stutzmann, A. Flöter, R. Zachai, X. Jiang and C.-P. Klages: *Photoconductivity of undoped, nitrogen-and boron-doped CVD-and synthetic diamond*, Diamond and Related Materials **7**, 879 (1998).
- [37] K. Beha, A. Batalov, N. B. Manson, R. Bratschitsch and h. Leitenstorfer, A.: *Optimum Photoluminescence Excitation and Recharging Cycle of Single Nitrogen-Vacancy Centers in Ultrapure Diamond*, Physical Review Letters **109**, 097404 (2012).
- [38] B. J. Shields, Q. Unterreithmeier, N. De Leon, H. Park and M. D. Lukin: *Efficient readout of a single spin state in diamond via spin-to-charge conversion*, Physical Review Letters **114**, 136402 (2015).
- [39] E. Bourgeois, E. Londero, K. Buczak, J. Hruby, M. Gulká, Y. Balasubramaniam, G. Wachter, J. Stursa, K. Dobes, F. Aumayr, M. Trupke, A. Gali and M. Nesladek: *Enhanced photoelectric detection of NV magnetic resonances in diamond under dual-beam excitation*, Physical Review B **95**, 041402 (2017).
- [40] F. Fuchs, B. Stender, M. Trupke, D. Simin, J. Pflaum, V. Dyakonov and G. V. Astakhov: *Engineering near-infrared single-photon emitters with optically active spins in ultrapure silicon carbide*, Applied Physics Letters **6**, 7578 (2017).
- [41] T. C. Hain, F. Fuchs, V. A. Soltamov, P. G. Baranov, G. V. Astakhov, T. Hertel and V. Dyakonov: *Excitation and recombination dynamics of vacancy-related spin centers in silicon carbide*, Journal of Applied Physics **115**, 133508 (2014).

- [42] W. Götz, A. Schöner, G. Pensl, W. Suttrop, W. J. Choyke, R. Stein and S. Leibenzeder: *Nitrogen donors in 4H-silicon carbide*, Journal of Applied Physics **73**, 3332 (1993).
- [43] D. A. Hopper, R. R. Grote, A. L. Exarhos and L. C. Bassett: *Near-infrared-assisted charge control and spin readout of the nitrogen-vacancy center in diamond*, Physical Review B **94**, 241201 (2016).

Danksagung

Viele Personen haben mich während meiner Forschungszeit am WSI begleitet und unterstützt, denen ich hier meinen herzlichen Dank aussprechen möchte:

Prof. Dr. Martin S. Brandt für die fachliche Betreuung meiner Arbeit sowie die Begleitung meines letzten Studienabschnitts als Mentor und Arbeitgeber. Dank ihm durfte ich erleben, wie aus einer einfachen Kugelschreiberskizze auf Papier kleines Laserlabor entsteht.

Prof. Dr. Martin Stutzmann für die Möglichkeit, am WSI zu forschen. Der Dank umfasst die Gewährleistung der ausgezeichneten Forschungsmöglichkeiten, die im Walter Schottky Institut geboten sind.

Florian Hrubesch für die persönliche Betreuung meiner Arbeit, für das Einbringen seines umfassenden Wissens während des Aufbaus des NV⁻-Spektrometers, sowie die an den Tag gelegte Motivation und Geduld, die für das Erreichen wissenschaftlicher Ziele unumgänglich ist.

David Franke, Anton Greppmair, Dr. Alexander Kupijaj, Natalie Galfe, Lukas Stelzer, Sebastian Simeth, Gerstberger Caroline und allen anderen ehemaligen Mitgliedern der Brandt Gruppe für die angenehme Arbeitsatmosphäre sowie die allzu häufige Erbringung des Beweises, dass kein Thema nicht diskussionswürdig ist.

Joana Figueiredo für die bemerkenswerte Gabe, stets Überblick und Kontrolle über alle bürokratischen Vorgänge zu haben.

Allen MitarbeiterInnen und WissenschaftlerInnen am WSI, Dank derer das WSI zu einem funktionierenden, kollegialen und produktiven Ort der Forschung wird.

Meinem dieses Jahr verstorbenen Opa für seine an den Tag gelegte Lebenskunst, seinen Geist und Witz. Mögest du in Frieden ruhen.

Bibliography

Meinen Freunden, meiner Familie und Verwandten, die mich während meiner Studienzeit begleitet und unterstützt haben. Besonders auch meinen **WG-Mitbewohnern** für jedes einzelne Wochenende, an dem unser Küchentisch zu einem Spielbrett wurde.

Claudia und Klaus Hartz für die Geduld in der Finanzierung meines Studiums, das jederzeit offene Ohr und einfach dafür, dass es sie gibt.

Meiner Freundin **Linh** für all das, was mir die Physik nicht geben kann.

Erklärung der Selbstständigkeit

Ich versichere hiermit, dass ich die von mir eingereichte Abschlussarbeit selbstständig verfasst und keine anderen als die angegebenen Quellen und Hilfsmittel benutzt habe.

.....
Ort, Datum

.....
Unterschrift